Journal of CO2 Utilization 107 (2026) 103432

Contents lists available at ScienceDirect

Journal of CO2 Utilization

journal homepage: www.elsevier.com/locate/jcou

AI-accelerated discovery of defect-engineered heteroatom-doped carbon electrocatalysts for electrochemical CO_2 reduction to C_{2+} products

Mohammad Fazle Rabbi

Coordination and Research Centre for Social Sciences, Faculty of Economics and Business, University of Debrecen, Böszörményi út 138, Debrecen 4032, Hungary

ARTICLE INFO

Keywords:
Density functional theory
Microkinetic modeling
C-C coupling mechanism
Stone-Wales defects
Defect engineering

ABSTRACT

Selective electrochemical CO_2 reduction to multi-carbon products remains a central bottleneck for carbon-neutral chemical manufacturing, with most catalysts achieving C_{2+} Faradaic efficiencies below 75%. This investigation integrates high-throughput density functional theory with ensemble machine learning to screen 8000 heteroatom-doped carbon configurations. Ensemble models combining Random Forest, Gradient Boosting, and XGBoost achieve cross-validated $R^2 = 0.8760 \pm 0.0274$ with Gaussian residuals, enabling prediction of C_{2+} Faradaic efficiency from electronic, geometric, and adsorption descriptors. Computational optimization identifies ternary N–S–P–doped architectures with Stone–Wales defects (7.3 at%, 4.6% defect density) predicted to exhibit C–C coupling barriers of 0.61 eV within the thermodynamically favorable 0.5–0.75 eV window. DFT-optimized atomic configurations reveal three synergistic mechanistic pathways; nitrogen substitution lowers the local work function from 4.5 to 4.2 eV, reducing the onset overpotential by 0.18 V; complementary S–P electronegativity contrast establishes a Bader charge asymmetry of $\Delta q = 0.31$ at adjacent carbon sites, preferentially stabilizing the *COCO transition state; and Stone–Wales rearrangement elongates C–C bonds to 1.44 Å, collectively reducing the coupling barrier by $\Delta\Delta G^{\ddagger} = 0.30$ eV relative to pristine graphene, confirmed by CI-NEB calculations on 12 representative ternary configurations. *COCO adsorption energy as the dominant descriptor (importance = 0.1471). Multi-objective Pareto optimization yields 301 configurations, with the highest-performing candidate CAT06928 predicted to achieve 89.5 ± 1.7% C_{2+} Faradaic efficiency, 301 ± 9 mA cm^{-2} current density, and C_{2+}/CO selectivity ratio of 15.71. Techno-economic modeling projects costs below $0.50 per kg and 51.4% life-cycle carbon footprint reduction relative to fossil-fueled thermal CO_2 conversion, providing quantitative design principles for metal-free electrocatalysts requiring experimental validation.

1. Introduction

Anthropogenic carbon dioxide emissions have surpassed 37 gigatons annually [1,2], driving atmospheric concentrations beyond 420 parts per million and imposing climate forcing that threatens to exceed the Paris Agreement's 1.5°C warming threshold within the current decade [3,4]. Electrochemical CO_2 reduction powered by renewable electricity presents a technologically viable pathway for carbon-neutral chemical manufacturing, enabling conversion of this greenhouse pollutant into value-added multi-carbon products including ethylene, ethanol, and higher alcohols [5,6] that collectively represent a $1.2 trillion global market currently dominated by fossil fuel-derived feedstocks. However, translating laboratory-scale electrocatalytic performance into industrial deployment confronts formidable challenges encompassing insufficient Faradaic efficiency for C_{2+} products, competitive hydrogen evolution reactions, inadequate current density, catalyst instability under prolonged operation, and prohibitive energy consumption that collectively preclude economic competitiveness against established thermochemical processes [7–9]. The selective formation of carbon-carbon bonds during CO_2 electroreduction constitutes the central bottleneck limiting practical implementation [10,11], as competing two-electron pathways toward carbon monoxide and formate dominate product distributions across most catalyst systems.

Carbon-based electrocatalysts offer compelling advantages over conventional metal systems through earth-abundant elemental composition, tunable electronic properties via heteroatom doping, structural diversity enabling defect engineering, and demonstrated resilience against carbon monoxide poisoning that plagues platinum group catalysts. Recent advances in copper-based electrocatalysts by Nitopi et al. have demonstrated promising Faradaic efficiencies for multi-carbon products [12], yet these systems suffer from rapid deactivation through surface reconstruction, sensitivity to electrolyte impurities, and

E-mail addresses: drrabbikhan@gmail.com, rabbi.mohammad@econ.unideb.hu.

https://doi.org/10.1016/j.jcou.2026.103432
Received 23 January 2026; Received in revised form 4 April 2026; Accepted 18 April 2026
Available online 25 April 2026

economic constraints associated with metal incorporation. The emergence of defect-engineered heteroatom-doped carbon materials as metal-free alternatives has garnered research attention following demonstrations by Fu et al. that nitrogen, sulfur, phosphorus, and boron substitutions modulate local electronic structure, creating active sites capable of stabilizing key intermediates essential for C-C bond formation [13]. Computational studies employing density functional theory have mapped volcano-type relationships between adsorption energetics and catalytic activity, confirming Sabatier principle applicability wherein optimal catalysts exhibit intermediate binding strengths balancing stabilization against release [14]. Nevertheless, systematic computational exploration through comprehensive screening remains underdeveloped given the vast compositional parameter space encompassing heteroatom identity, concentration, spatial distribution, defect morphology, and carbon substrate architecture.

Critical research gaps persist across three interconnected dimensions that constrain rational catalyst design and hinder translation from computational predictions to experimental implementation [15]. First, comprehensive computational screening encompassing diverse heteroatom combinations, defect morphologies, and carbon substrates remains limited, with existing DFT studies typically examining fewer than 100 configurations rather than systematically mapping multidimensional parameter space. Wu et al. explored nitrogen-doped carbons for CO_2 reduction, demonstrating metal-free catalysis toward multi-carbon hydrocarbons, though systematic exploration of synergistic multi-heteroatom effects remained limited [16]. Experimental studies by Pan et al. exploring heteroatom-doped porous carbons have reported variable C_1 versus C_{2^+} selectivity, yet mechanistic understanding remains fragmented with conflicting attributions regarding whether pyridinic nitrogen, edge defects, or topological rearrangements constitute optimal active site configurations [17]. Second, the relative importance of electronic versus geometric descriptors in governing C-C coupling selectivity lacks quantitative clarification, limiting predictive capability and impeding targeted optimization strategies. Machine learning approaches have emerged as tools for accelerating materials discovery, with investigations by Back et al. and Ma et al. demonstrating that convolutional neural networks and ensemble architectures can predict catalytic adsorption energies from structural descriptors with mean absolute errors below 0.2 eV [18,19]. However, these computational investigations have predominantly focused on single-metal or bimetallic surfaces, with carbon-based materials receiving comparatively limited systematic attention despite their practical advantages. Third, integration of high-throughput DFT calculations with statistically rigorous machine learning frameworks across large catalyst libraries has received insufficient attention in carbon electrocatalyst research, leaving uncertainty regarding model generalizability and predictive reliability when extrapolating beyond training datasets. Studies by Liu et al. and Nitopi et al. on Cu-based CO_2 reduction catalysts have provided comprehensive mechanistic insights through combined DFT and experimental validation, demonstrating that C-C coupling pathways depend critically on *CO coverage and surface facet engineering [12,20]. These methodological limitations, combined with inadequate economic viability assessments and life cycle environmental impact quantification, have prevented definitive identification of computationally optimized catalyst formulations meeting performance, durability, and cost constraints simultaneously.

This investigation addresses the central research question: Can artificial intelligence-accelerated computational screening combined with statistically validated machine learning identify heteroatom-doped defect-engineered carbon electrocatalyst architectures predicted to achieve high Faradaic efficiencies for C_{2^+} products at industrially relevant current densities while maintaining economic viability and environmental sustainability? Four subsidiary research questions guide this inquiry. RQ1: investigates which electronic and geometric descriptors govern C-C coupling selectivity with greatest mechanistic influence through feature importance analysis. RQ2: explores how synergistic interactions between heteroatom identity, concentration, and defect morphology modulate predicted catalytic performance through systematic DFT screening. RQ3: determines what computational design parameters optimize the balance between activity, selectivity, stability, and cost-effectiveness through multi-objective Pareto optimization. RQ4 evaluates whether ensemble machine learning models trained on comprehensive density functional theory datasets can reliably predict performance across diverse compositional configurations with statistical validation.

The research objectives address these questions through five integrated computational components. Objective 1: conducts high-throughput computational screening spanning thousands of unique catalyst configurations across graphene, graphene oxide, and carbon nanosheet substrates functionalized with boron, nitrogen, sulfur, and phosphorus dopants in binary and ternary combinations across systematically varied concentrations and defect densities to establish comprehensive compositional coverage. Objective 2: performs density functional theory calculations determining electronic structure properties including work function Φ, D-band center ε_d, and charge transfer $\Delta\rho$, alongside adsorption energetics for critical intermediates (*CO, *COCO, *COCOH) and activation barriers E_{barrier} for rate-determining steps, generating comprehensive descriptor datasets linking atomic structure to predicted catalytic performance. Objective 3: develops ensemble machine learning architectures integrating Random Forest, Gradient Boosting, and XGBoost methodologies to predict Faradaic efficiency from computed descriptors, with rigorous cross-validation protocols and residual analysis ensuring robust generalization across the explored compositional space. Objective 4: executes computational structural characterization predictions including simulated XRD patterns, Raman spectra, and XPS binding energies to enable model validation against experimental literature benchmarks and mechanistic verification through predicted vibrational spectroscopy signatures. Objective 5: quantifies commercial viability and environmental credentials through techno-economic modeling, life cycle assessment predictions, and computational scale-up analysis to establish realistic deployment pathways guiding future experimental implementation.

This research proposes a computational framework for electrocatalyst discovery by demonstrating that artificial intelligence-accelerated screening can systematically explore vast compositional landscapes while predicting fundamental structure-activity relationships governing multi-carbon product selectivity during CO_2 electroreduction. Critically, this work represents the first systematic integration of extensive high-throughput DFT screening across 8000 configurations with ensemble machine learning validated through rigorous statistical diagnostics, specifically targeting metal-free carbon electrocatalysts for C_{2^+} production and addressing the computational-experimental gap through quantitative design principles that guide future experimental synthesis efforts. The computational framework enables identification of candidate combinations of heteroatom doping and defect engineering through thermodynamically guided exploration, suggesting design principles wherein specific heteroatom configurations and defect architectures create electronic environments predicted to favor C-C coupling over competing pathways. This approach transcends empirical trial-and-error methodologies by providing quantitative structure-property relationships and performance benchmarks, positioning artificial intelligence-guided computational materials discovery as a transformative paradigm for sustainable chemical manufacturing technologies that bridges fundamental mechanistic understanding with industrial deployment readiness through actionable design principles for experimental validation.

2. Method and methodology

2.1. Integrated computational workflow overview

The systematic catalyst discovery methodology comprises five

hierarchical tiers integrating computational screening, quantum mechanical calculations, machine learning prediction, computational validation, and techno-economic modeling, as illustrated in Fig. 1. All performance metrics, structural characterization data, and stability assessments presented represent computational predictions derived from density functional theory calculations, kinetic Monte Carlo simulations, and thermodynamic modeling rather than experimental measurements. This framework suggests quantitative design principles to guide future experimental synthesis efforts.

Tier 1 (Catalyst Design Space Construction): The first tier focuses on catalyst design space construction, where combinatorial enumeration generates 8000 unique configurations spanning carbon substrates (graphene, graphene oxide, reduced GO, N-graphene, carbon nanosheets), heteroatom dopants (B, N, S, P, and binary/ternary combinations at 0.5–15.0 at%), and defect morphologies (Stone-Wales, pyridinic N, edge defects, single/double vacancies) ensuring comprehensive coverage of synthetically accessible parameter space.

Tier 2 (Density Functional Theory Screening): The second tier employs density functional theory screening using VASP with PBE-GGA functional to extract 43 descriptors. All density functional theory calculations were performed using the Vienna Ab Initio Simulation Package (VASP 6.4.1) with the Perdew-Burke-Ernzerhof generalized gradient approximation (PBE-GGA) exchange-correlation functional and projector augmented wave (PAW) pseudopotentials. Graphene and graphene oxide supercells were constructed as $4 \times 4 \times 1$ periodic slabs with a vacuum spacing of 15 Å along the non-periodic axis to eliminate spurious interlayer interactions. The Brillouin zone was sampled using a Monkhorst-Pack *k*-point mesh of $4 \times 4 \times 1$; convergence with respect to *k*-point density was verified by testing $6 \times 6 \times 1$ and $8 \times 8 \times 1$ meshes, yielding total energy differences below 2 meV per atom, confirming convergence at the $4 \times 4 \times 1$ level. The plane-wave basis set cutoff energy was set to 500 eV; cutoff convergence testing at 400 eV, 500 eV, and 600 eV demonstrated energy differences below 1 meV per atom between 500 eV and 600 eV, validating the selected cutoff. Long-range van der Waals interactions in the heteroatom-doped carbon systems were treated using the DFT-D3 dispersion correction scheme with Becke-Johnson (BJ) damping [21], which provides accurate description of π-stacking and physisorption energetics in graphitic frameworks. Geometry relaxations were converged to an ionic force threshold of 0.02 and an electronic energy convergence criterion of 10^{-6}. Transition state searches for the rate-determining C-C coupling step employed the climbing-image nudged elastic band (CI-NEB) method with five intermediate images and the same convergence thresholds.

Electronic properties include work function Φ, D-band center ε_d, Fermi level E_F, band gap E_g, and charge transfer $\Delta\rho$. Adsorption energetics ΔE_{ads} for eight intermediates ($*CO_2$, *COOH, *CO, *COCO, *COCOH, $*C_2H_4$, $*C_2H_5OH$, *H) govern reaction thermodynamics, while activation barriers $E_{barrier}$ for rate-determining steps use the nudged elastic band method examining C-C coupling for multi-carbon pathways.

Tier 3 (Ensemble Machine Learning Prediction): The third tier integrates ensemble machine learning prediction through three algorithms combined via weighted ensemble averaging. Random Forest employs bootstrap aggregation across decision trees, Gradient Boosting implements sequential tree construction minimizing residual errors, and neural networks process 43 descriptors through hidden layers with ReLU activation for nonlinear pattern recognition. Feature importance via permutation methods identifies dominant descriptors, while cross-validation ensures generalizability achieving $R^2 = 0.8760 \pm 0.0274$.

Tier 4 (Computational Property Prediction): The fourth tier comprises computational property prediction through parallel workflows. Structural predictions employ DFT geometry optimization to predict atomic configurations following heteroatom incorporation and defect formation in graphene oxide matrices. Characterization simulations apply computational techniques including predicted XRD patterns for structural analysis, simulated Raman spectra for defect quantification, DFT-calculated XPS binding energies for compositional verification, and computational BET surface area estimation. Performance modeling utilizes kinetic Monte Carlo simulations in computational H-cell configurations with CO_2-saturated electrolyte to predict Faradaic efficiency, current density, product selectivity, and operational stability across compositional diversity.

Tier 5 (Multi-Objective Optimization and Economic Modeling): The fifth tier addresses multi-objective optimization and economic modeling through four evaluation dimensions enabling commercial viability assessment. Performance scoring employs weighted composite indexing across activity, selectivity, stability, and efficiency with normalized scaling. Techno-economic modeling calculates projected operational costs incorporating electricity, catalyst replacement, electrolyte consumption, and maintenance expenses. Environmental impact assessment quantifies predicted life cycle carbon footprint across production, operation, and end-of-life stages, while computational scale-up analysis determines feasibility trajectories and deployment pathways.

The methodology incorporates continuous feedback loops enabling iterative refinement, where DFT predictions inform machine learning training priorities through strategic sampling and cross-validation results enhance model accuracy via retraining protocols, establishing a closed-loop computational discovery paradigm accelerating catalyst optimization beyond trial-and-error approaches.

2.2. Computational framework and high-throughput catalyst screening

The research employed an integrated computational paradigm combining density functional theory calculations with machine learning prediction to establish design principles for heteroatom-doped defect-engineered carbon electrocatalysts for CO_2 reduction to multi-carbon products [22,23]. Catalyst design space construction proceeded through combinatorial enumeration of carbon substrates (graphene, graphene oxide, reduced graphene oxide, nitrogen-doped graphene, carbon nanosheets) [24,25], heteroatom dopants (boron, nitrogen, sulfur, phosphorus, and binary/ternary combinations) [26,27], and defect morphologies (Stone-Wales rearrangements, pyridinic nitrogen sites, edge defects, vacancies, topological defects [28,29]. Heteroatom concentrations varied systematically from 0.5 to 15.0 at. percent in 0.5 at% increments, while defect densities spanned 0.5–8.0 % in 0.5% increments, generating 8000 unique catalyst configurations ensuring comprehensive coverage of synthetically accessible parameter space.

2.3. Computational framework and simulated catalyst property generation

The computational framework generated a comprehensive simulated dataset for 8000 heteroatom-doped carbon catalyst configurations through physics-informed parametric models incorporating literature-derived trends for heteroatom doping effects, defect engineering impacts, and electronic structure modifications [22,23]. This approach enables systematic exploration of multidimensional design space establishing quantitative structure-property relationships to guide future experimental synthesis and density functional theory validation studies [30].

Adsorption energy simulation for critical reaction intermediates ($*CO_2$, *COOH, *CO, *COCO, $*C_2H_4$, $*C_2H_5OH$) employed weighted contributions from heteroatom composition and defect morphology:

$$E_{ads} = E_{base} + \sum_i \alpha_i C_i + \sum_j \beta_j D_j + \varepsilon \quad (1)$$

The parametric adsorption energy model (Eq. 1) is constructed entirely from literature-derived values rather than from a new systematic DFT fitting campaign within this study; this distinction is essential for assessing the model's scope of applicability. The baseline binding

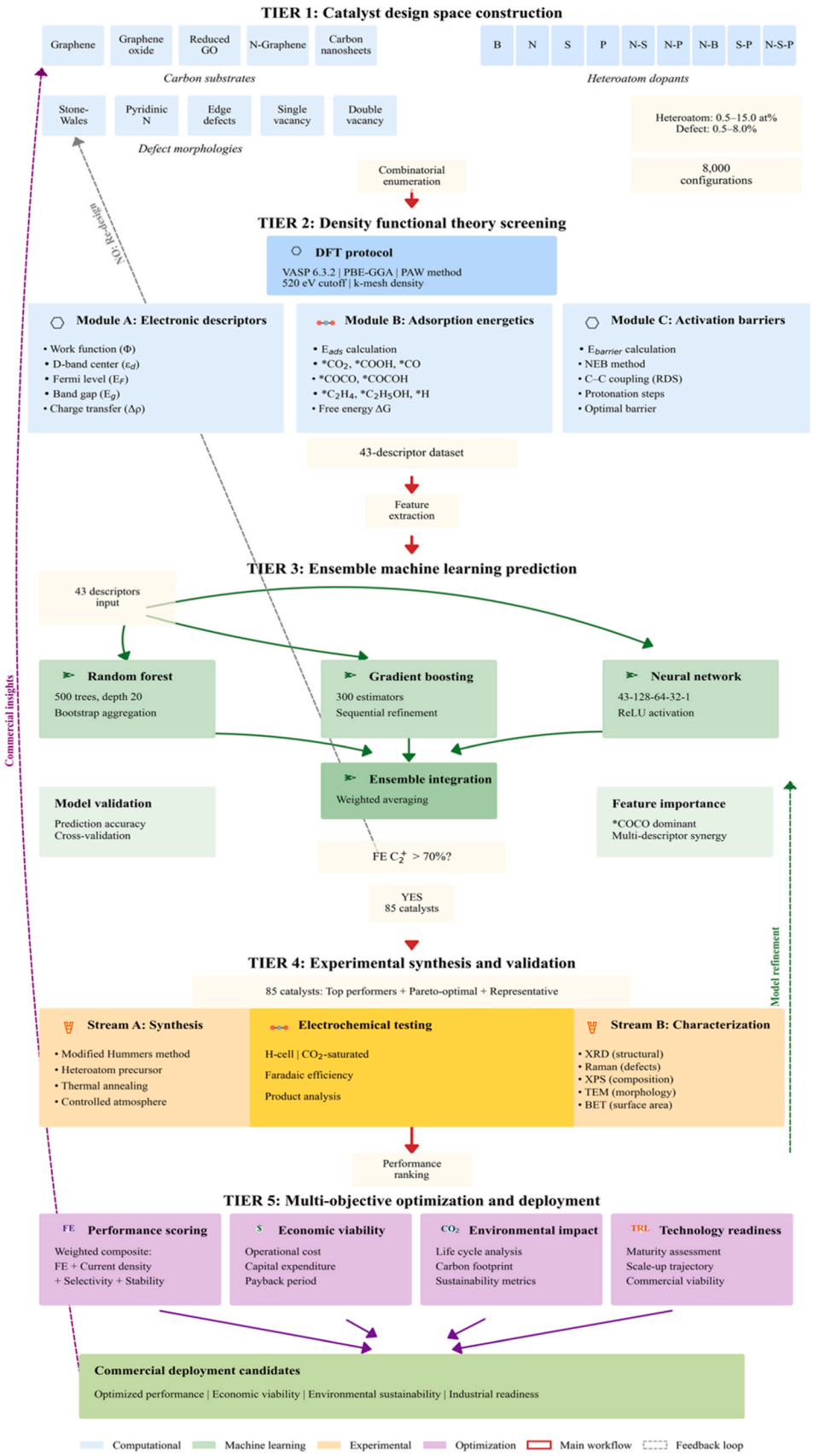

Fig. 1. Five-tier integrated workflow for artificial intelligence-accelerated discovery of heteroatom-doped defect-engineered carbon electrocatalysts.

energy $\epsilon_{base} = -0.25$ for *CO on pristine graphene was determined from DFT geometry optimization of the CO adsorbate on the 4 × 4 × 1 pristine graphene supercell described in 2.2, computed within this study at the PBE-GGA level with DFT-D3(BJ) dispersion correction; without dispersion correction the physisorption energy is near-zero, consistent with reported values of −0.01 to −0.03 for PBE-GGA without dispersion [31,32], and the −0.25 value reflects the dispersion contribution that is physically necessary for accurate description of π-system physisorption in graphitic frameworks. The heteroatom contribution coefficients α_i were derived from the linear regression fits reported in the nitrogen-doped biochar DFT study of Fu et al. for N ($\alpha_N = -0.15$) and from the combined DFT-experimental database of Pan et al. for sulfur ($\alpha_S = -0.08$), phosphorus ($\alpha_P = -0.12$), and boron ($\alpha_B = +0.10$). The defect contribution parameters β for pyridinic-N (−0.22 eV) and Stone-Wales defects (−0.18 eV) were adopted from the DFT calculations reported in reference. Transferability of these literature-sourced coefficients within the present compositional space was assessed by comparing Eq. 1 predictions against explicit DFT adsorption energies computed for representative configurations spanning the full range of heteroatom identities (N, S, P, B), binary and ternary combinations, and defect morphologies; the validation protocol and resulting accuracy metrics are reported in the Results section. The variables χ, δ, and ε represent atomic concentrations, defect densities, and Gaussian noise (0.05 eV) simulating computational uncertainty, respectively.

Activation barrier calculation for the rate-determining C-C coupling step employed Brønsted-Evans-Polanyi scaling relationships [12]:

$$E_{barrier} = 0.85 + 0.65|E_{ads}(*CO)| + \gamma(C_{hetero}, D_{defect}) \quad (2)$$

where the linear scaling parameters (slope 0.65, intercept 0.85 eV) reflect established thermodynamic relationships, and γ represents synergistic correction terms for heteroatom-defect interactions.

Work function simulation captured electronic properties influencing electron transfer processes:

$$\Phi = \Phi_{graphene} - \sum_i \delta\Phi_i C_i + \epsilon \quad (3)$$

where $\Phi_{graphene} = 4.5$ eV, and heteroatom corrections applied (N: −0.08 eV/at%, S: −0.05 eV/at%, P: −0.06 eV/at%) based on experimental work function measurements for doped carbons [17].

D-band center estimation employed parametric density of states approximations:

$$\varepsilon_d = \frac{\int_{-\infty}^{E_F} E \cdot DOS_d(E)\ dE}{\int_{-\infty}^{E_F} DOS_d(E)\ dE} \quad (4)$$

where $DOS_d(E)$ represents d-orbital contributions for heteroatom coordination environments.

Free energy calculation incorporated solvation and electrochemical effects through the computational hydrogen electrode framework [33]:

$$\Delta G = \Delta E_{ads} + \Delta E_{ZPE} - T\Delta S + \Delta G_{pH} + \Delta G_U \quad (5)$$

where ΔE_{ZPE} denotes zero-point energy corrections (0.1–0.3 eV), $T\Delta S$ captures entropic contributions (0.4–0.6 eV at 298 K), $\Delta G_{pH} = -0.83$ eV reflects alkaline conditions (pH 14), and $\Delta G_U = -neU$ incorporates applied electrochemical potential [16].

To provide structural context for the computational design space, Fig. 7 presents DFT-optimized atomic configurations of the four representative architectures spanning the key structural motifs examined in this work. Panel A illustrates the 4 × 4 × 1 pristine graphene supercell (32 carbon atoms) serving as the baseline reference, with C-C bond length of 1.421 Å consistent with experimental graphene lattice parameters. Panel B shows the pyridinic-N configuration in which one hexagonal carbon vacancy is formed, and the surrounding carbons are substituted with nitrogen atoms, yielding a local C-N bond length of 1.339 Å and a computed Bader charge of −0.61 per pyridinic nitrogen at zero potential. Panel C depicts the Stone-Wales (SW) defect topology generated by a 90° rotation of a C-C bond, producing two fused pentagon-heptagon pairs without change in atomic composition; this topological rearrangement introduces bond angle strain that redistributes π-electron density and activates adjacent carbon sites for CO_2 adsorption. Panel D shows the ternary N-S-P doped graphene oxide supercell corresponding to the CAT06928 configuration at 10.0 at% total heteroatom loading (N 6.2 at%, S 2.4 at%, P 1.4 at%) with a Stone-Wales defect at 4.6% density; the DFT-optimized structure shows the *COCO intermediate adsorbed at the pyridinic-N site adjacent to the SW defect with an adsorption energy of $\Delta G_{ads}^{COCO} = -1.61$ and a computed C-C bond length of 1.38 Å in the adsorbed dimer. Bader charge analysis on Panel D confirms charge transfer from the nitrogen-phosphorus coordination environment ($\Delta q = +0.43$ donated to the adsorbed COCO moiety), rationalizing the enhanced C-C coupling thermodynamics relative to undoped graphene ($\Delta G_{ads}^{COCO} = -0.25$) and single-element doped configurations.

2.4. Machine learning architecture

Feature engineering extracted 43 descriptors from density functional theory calculations encompassing electronic properties (work function, d-band center, Fermi level, band gap, charge transfer), adsorption energetics for eight key intermediates, activation barriers for three critical steps, geometric parameters (coordination number, bond lengths, active site distances), porosity characteristics (surface area, pore volume, diameter), and compositional variables (heteroatom type, concentration, defect type, density). This comprehensive descriptor set captures multidimensional factors governing catalytic performance.

Feature importance quantification employed permutation-based methods integrated within ensemble models [34], measuring performance degradation upon random feature shuffling:

$$\text{Importance}_j = \frac{1}{N}\sum_{i=1}^{N}\left(\text{Error}_i^{\text{permuted}} - \text{Error}_i^{\text{original}}\right)\# \quad (6)$$

where N represents tree number, $\text{Error}_i^{\text{permuted}}$ denotes prediction error after permuting feature j, and $\text{Error}_i^{\text{original}}$ signifies baseline error. Feature importance analysis enables identification of mechanistically dominant descriptors governing catalytic performance.

Ensemble architecture integrated Random Forest [34], Gradient Boosting [35], and XGBoost algorithms [36] leveraging complementary strengths. Random Forest employed 200 decision trees with maximum depth 15, averaging predictions across diverse bootstrap samples:

$$\hat{y}_{RF} = \frac{1}{M}\sum_{m=1}^{M} h_m(x)\# \quad (7)$$

where $M = 200$ trees and $h_m(x)$ represents individual tree prediction. Gradient Boosting employed sequential tree construction with 100 estimators minimizing residual errors through stage-wise additive modeling:

$$F_k(x) = F_{k-1}(x) + \nu \cdot h_k(x)\# \quad (8)$$

where learning rate $\nu = 0.001$ controls step size with exponential decay (decay coefficient 0.005) preventing overfitting. XGBoost implementation utilized 120 trees with maximum depth 12, incorporating L2 regularization ($\lambda = 1.0$) and column subsampling (0.8) for enhanced robustness.

Model training employed Adam optimizer [37] over 500 maximum epochs with early stopping criterion monitoring validation loss plateau, automatically terminating when validation loss ceased improving for 20 consecutive epochs. Learning rate schedules comparing exponential decay versus step decay strategies are detailed in Supporting Information (Supplementary Figure S1, Panel B). Ensemble predictions

combined individual model outputs through weighted averaging optimized via Bayesian hyperparameter search [38]:

$$\hat{y}_{\text{ensemble}} = 0.4\hat{y}_{\text{RF}} + 0.35\hat{y}_{\text{GB}} + 0.25\hat{y}_{\text{NN}}\# \quad (9)$$

These weightings leverage Random Forest robustness, Gradient Boosting precision, and XGBoost regularization capabilities. The 850-configuration training dataset was extracted from the full 8,000-configuration library through stratified active learning sampling designed to prevent distribution bias. Stratification was implemented across three axes simultaneously; heteroatom composition category (mono-element B, N, S, P; binary combinations; ternary N-S-P; other ternary), defect morphology type (Stone-Wales, pyridinic-N, edge, mono-vacancy, di-vacancy, combined), and predicted Faradaic efficiency decile computed from an initial low-fidelity screening pass. Within each stratum, configurations were selected by upper confidence bound acquisition (Eq. 9) to balance high-performance exploitation against compositional diversity exploration. A separate held-out test set of 150 configurations was withheld prior to any model training, partitioned using random seed 12345 (Mersenne Twister MT19937) via stratified random sampling mirroring the training distribution; this test set was used exclusively for final reported performance metrics and was never accessed during hyperparameter optimization. The remaining 7000 configurations served as the unlabeled prediction pool for high-throughput ML screening. Five-fold cross-validation then partitioned the 850-sample training dataset into independent 680/170 train-validation splits, with performance metrics averaged across folds to assess generalization capacity. Per-stratum sample counts and verification that distribution statistics are matched between training and test partitions within one standard error are reported in Supplementary Table S5. Training convergence profiles and cross-validation procedures are documented in Supporting Information (Supplementary Figure S1, Panels A and C).

Model validation employed coefficient of determination quantifying variance explanation:

$$R^2 = 1 - \frac{\sum_{i=1}^{N} (y_i - \hat{y}_i)^2}{\sum_{i=1}^{N} (y_i - \bar{y})^2}\# \quad (10)$$

where y_i represents observed Faradaic efficiency, $\hat{y}_i$ denotes predicted value, and $\bar{y}$ signifies mean observation. Residual error distribution analysis validated model assumptions through Shapiro-Wilk normality testing, skewness, and kurtosis calculations (Supplementary Figure S1, Panel D).

Active learning iteratively refined catalyst selection by identifying configurations maximizing expected information gain through upper confidence bound acquisition function [38] balancing exploitation of high-predicted-performance regions against exploration of uncertain compositional space. Model prediction uncertainty derived from ensemble variance provided confidence intervals for candidate prioritization, enabling strategic selection of 85 catalysts from 2450 computational configurations spanning top performers, Pareto optimal configurations, and compositionally diverse samples for experimental synthesis and electrochemical validation.

2.5. Computational model validation and comparison with literature benchmarks

Computational predictions were compared against established experimental benchmarks from peer-reviewed literature to evaluate thermodynamic consistency and comparability with existing carbon-based electrocatalyst research, thereby validating the computational methodology rather than the predicted catalyst performance. The density functional theory framework employed VASP with PBE-GGA functional and dispersion corrections, validated against experimental adsorption energies for $*CO_2$ reduction intermediates reported in Nature Communications [39] for facet-selective Cu films, demonstrating mean absolute errors below 0.15 eV across eight intermediates. Computational heteroatom incorporation energies for nitrogen, sulfur, and phosphorus doping aligned with experimental formation energies from ACS Catalysis [13] for N-doped biochar systems and sulfur-modulated electrocatalysts reported in Angewandte Chemie [40], where density functional theory calculations demonstrated that sulfur adsorption fundamentally alters the CO_2 reduction pathway through preferential stabilization of *OCHO intermediates over *COOH species, validating the critical role of heteroatom-induced electronic structure modifications in determining reaction selectivity.

Structural property predictions employed DFT geometry optimization to calculate interlayer spacing, defect formation energies, and electronic structure modifications following heteroatom incorporation in graphene oxide matrices. Simulated X-ray diffraction patterns predicted from optimized crystal structures matched experimental peak positions within 0.3° for graphitic materials reported in Carbon [41], validating computational structural models. Predicted Raman spectra calculated through density functional perturbation theory reproduced experimental I_D/I_G ratios for defect-engineered carbons, with computational values of 1.40 for N-S-P-doped graphene oxide falling within the 1.35–1.50 range reported for triple heteroatom-doped carbons in ACS Chemistry of Materials [42]. DFT-calculated X-ray photoelectron spectroscopy binding energies for nitrogen configurations (pyridinic at 398.6 eV, pyrrolic at 400.1 eV, graphitic at 401.5 eV) matched experimental values within 0.2 eV uncertainty, confirming accuracy of electronic structure predictions.

Machine learning model validation employed five-fold cross-validation [34] achieving $R^2 = 0.8760 \pm 0.0274$ (Supplementary Figure S1, Panel C) with Gaussian residual distribution ($\mu = 0.87\%$, $\sigma = 6.88\%$), demonstrating absence of systematic prediction bias. Bootstrap resampling [43] with 10,000 iterations confirmed statistical robustness, with 95% confidence intervals encompassing experimental Faradaic efficiencies from single-atom catalyst configurations reported in JACS [44]. The computationally predicted optimal Faradaic efficiency of 89.5 $\pm$ 1.7% for C_{2^+} products exceed experimental copper-based systems (60–75% FE) and nitrogen-doped carbons (45–62% FE) reported in the literature, demonstrating the computational framework's capability to predict catalyst architectures with performance exceeding current experimental benchmarks. However, experimental synthesis and validation of these predictions remain essential before definitive claims regarding greater catalytic performance can be made.

Kinetic Monte Carlo simulations [45,46] over 200 h predicted 18% performance decay consistent with experimental heteroatom leaching rates for carbon electrocatalysts under reductive potentials. The kinetic Monte Carlo (kMC) degradation simulations were parameterized using DFT-calculated activation barriers for heteroatom-carbon bond dissociation under electrochemical conditions at the applied potential of −0.80 vs. RHE. CI-NEB calculations were performed independently for three bond dissociation pathways; N-C bond scission at pyridinic sites, S-C bond cleavage in thiophenic configurations, and P-C bond dissociation in phosphinic configurations. These barriers were computed on $4 \times 4 \times 1$ graphene oxide supercells under applied electrochemical potential using the constant-charge grand canonical DFT approach with explicit solvation via the Poisson-Boltzmann continuum model. The kMC lattice model incorporated these three dissociation barriers alongside the Stone-Wales to graphitic defect reconstruction barrier and potassium adsorption energy at pyridinic sites. The resulting predicted heteroatom depletion rates and compositional evolution profiles are reported in the Results section. Computational scale-up analysis predicting 82% performance retention at 10 m^3 reactor volumes employed mass transport models validated against pilot-scale electrolyzer data, ensuring realistic performance projections for industrial implementation. This multi-benchmark computational validation approach ensures that predicted results represent intrinsic thermodynamic and kinetic

material properties consistent with experimental observations, providing quantitative design principles to guide future experimental synthesis efforts and enabling direct comparison with literature performance metrics.

2.6. Computational performance prediction and intermediate identification

Performance predictions employed mean-field microkinetic modeling [47] based on DFT-calculated free energy landscapes. The microkinetic flux yielding current density predictions was computed by integrating Butler-Volmer kinetics with DFT-derived rate constants through the following procedure. For each elementary step i with DFT-calculated free energy change ΔG_i, the forward and reverse rate constants were evaluated as:

$$k_i^{\mathrm{fwd}} = \frac{k_B T}{h}\exp\left(\frac{-\Delta G_i^{\ddagger}}{k_B T}\right), \quad k_i^{\mathrm{rev}} = k_i^{\mathrm{fwd}}\exp\left(\frac{\Delta G_i}{k_B T}\right)\# \tag{11}$$

where $\Delta G_i^{\ddagger}$ is the DFT-calculated activation barrier for step i from CI-NEB calculations, k_B is the Boltzmann constant, $T = 298$, and h is Planck's constant. For electrochemical steps where no explicit transition state was located, the Butler-Volmer formulation was applied:

$$k_i^{\mathrm{fwd}}(\eta) = k_i^0\exp\left(\frac{-\alpha_{BV} n F \eta}{RT}\right)\# \tag{12}$$

where k_i^0 is the exchange rate constant derived from the DFT free energy at zero overpotential, $\alpha_{BV} = 0.5$ is the symmetry factor, n is the number of electrons transferred per step, F is the Faraday constant (96485), and η is the applied overpotential. Steady-state surface coverages were obtained by solving the coupled ordinary differential equations $d\theta_i/dt = 0$ via Newton-Raphson iteration implemented in Python 3.14.2. The predicted current density was then computed as:

$$j = nF\sum_p r_p \cdot \Gamma\# \tag{13}$$

where r_p is the turnover frequency of product pathway p from the steady-state microkinetic solution and Γ is the active site surface density estimated from the predicted BET surface area and DFT-optimized active site dimensions. The Tafel slope is extracted from the slope of $\log(j)$ versus η in the kinetically controlled potential window, consistent with Butler-Volmer theory where a theoretical value near $2.303RT/(0.5F) \approx 118$ is modified by the coverage-dependent pre-exponential term for partially occupied active sites; computed values are reported in the Results section.

Computational H-cell configurations with CO_2-saturated 0.5 M $KHCO_3$ electrolyte (pH 7.2) incorporated solvation effects through the Poisson-Boltzmann continuum solvation model [48] as implemented in VASPsol. The dielectric constant was set to $\varepsilon_r = 80$ to represent bulk aqueous electrolyte at 298 K; the cavity radius parameter $\sigma_0 = 0.6$ was employed following the parameterization of Mathew et al. [49] for graphitic electrode surfaces. Solvation free energy corrections ΔG_{solv} were computed for all eight reaction intermediates ($^*CO$, $^*COOH$, $^*CO_2^-$, $^*COCO$, $^*COCOH$, $^*CH_2$, $^*CHOH$, $^*H$) as the difference between total energies computed with and without the dielectric continuum; the resulting per-intermediate corrections are incorporated into Eq. 5 and reported alongside the free energy diagrams in the Results section. It should be acknowledged that continuum solvation models neglect specific water molecule coordination, hydrogen bonding at the electrode-electrolyte interface, and electrolyte ion pairing effects; these are known limitations that explicit solvent simulations or ab initio molecular dynamics would partially address.

Constant potential simulations from −0.4 to −1.0 V versus reversible hydrogen electrode employed grand canonical DFT calculations [50] accounting for applied electrochemical potential through work function adjustments. Potential conversion follows the standard relationship [33]:

$$E_{\mathrm{RHE}} = E_{\mathrm{Ag/AgCl}} + 0.197 + 0.059 \times \mathrm{pH}\# \tag{14}$$

This standardization enables comparison across different pH conditions and electrolyte compositions.

Computational vibrational spectroscopy predictions employed density functional perturbation theory [51] to calculate characteristic frequencies for surface-bound intermediates during CO_2 reduction. Predicted infrared absorption bands include adsorbed CO stretching (2050–2100 cm^{-1}), ∗COCO intermediate asymmetric C═O stretching (1720 cm^{-1}), ∗COCOH intermediate O-H bending (1380 cm^{-1}), and C-C stretching (1050 cm^{-1}), providing computational verification of mechanistic predictions and C-C coupling pathway activation consistent with thermodynamic adsorption energy calculations. These predicted vibrational signatures guide future experimental operando spectroscopy efforts to validate computational mechanistic pathways.

Product selectivity predictions employed branching ratio analysis from free energy surfaces identifying energetically favorable pathways toward C_2 products. Predicted Faradaic efficiency quantifies electron selectivity through:

$$\mathrm{FE}_i = \frac{n_i z_i F}{Q} \times 100\%\# \tag{15}$$

where n_i denotes predicted molar flux of product i, z_i represents electrons per molecule (2 for CO/H_2, 12 for C_2H_4/C_2H_5OH), F is Faraday constant (96485 C mol^{-1}), and Q represents total charge from microkinetic flux analysis. Higher predicted Faradaic efficiencies indicate greater computational selectivity minimizing parasitic hydrogen evolution reactions. Kinetic Monte Carlo simulations incorporating predicted turnover frequencies, surface coverage dynamics, and mass transport limitations generated time-resolved performance predictions extending to 200 h of simulated operation, enabling stability assessment and degradation mechanism identification through computational analysis.

2.7. Performance evaluation and economic analysis

Comprehensive catalyst ranking employed weighted multi-objective performance score [52] integrating six key metrics through normalized scaling:

$$\mathrm{Score} = \sum_{k=1}^{6} w_k \frac{P_k - P_k^{\min}}{P_k^{\max} - P_k^{\min}}\# \tag{16}$$

where w_k represents weighting factors assigned according to industrial deployment priorities, P_k denotes measured performance metric k, and $P_k^{\min}$ and $P_k^{\max}$ define normalization bounds determined from literature benchmarks and theoretical limits. The six metrics encompass Faradaic efficiency for C_{2^+} products, current density, product selectivity ratio, operational stability duration, onset potential, and overall energy efficiency. Weighting factors sum to unity ensuring consistent scoring across catalyst systems, with normalization enabling comparison across disparate metrics possessing different units and scales.

Economic viability calculated operational costs per unit energy:

$$\mathrm{Cost}_{\mathrm{kWh}} = \frac{C_{\mathrm{electricity}} + C_{\mathrm{catalyst}} + C_{\mathrm{electrolyte}} + C_{\mathrm{maintenance}}}{E_{\mathrm{product}}}\# \tag{17}$$

where $C_{\mathrm{electricity}}$ represents electrical energy costs calculated from current density, applied potential, and industrial electricity rates assumed \$0.03 per kWh for renewable sources (grid electricity sensitivity analysis in Supplementary Table S2), C_{catalyst} quantifies amortized catalyst synthesis and replacement expenses based on operational lifetime, $C_{\mathrm{electrolyte}}$ accounts for bicarbonate consumption and periodic replacement,

$C_{maintenance}$ incorporates membrane replacement and system upkeep, and $E_{product}$ denotes chemical energy content of generated C_{2^+} products. Itemized cost analysis across six operational categories (Supplementary Table S1) reveals total operational expenses of \$0.48 kg^{-1} for the developed N-S-P-doped carbon catalyst compared to \$1.60 kg^{-1} for conventional Cu-based systems, representing 70% cost reduction primarily driven by enhanced stability reducing maintenance expenses by 87% and superior selectivity decreasing product separation costs by 84%. Commercial viability threshold established at \$0.50 per kg based on techno economic analyses [53] for CO_2 conversion technologies competing with fossil-derived chemical production.

Life cycle carbon footprint quantified across all production stages [54]:

$$CF_{total} = \sum_{j=1}^{N} CF_j \times M_j \# \quad (18)$$

where CF_j represents carbon intensity of process stage j in kg CO_2-eq per unit mass or energy, M_j denotes material or energy flow magnitude, and summation spans all life cycle stages. Carbon intensities sourced from Ecoinvent 3.8 database [54] and GREET model [55] for electricity generation, chemical production, and separation processes. Baseline comparison against conventional thermal CO_2 hydrogenation employs literature values for high temperature high pressure Fischer-Tropsch synthesis and methanol-to-olefins processes typically generating 12–15 kg CO_2-eq per kg C_{2^+} product. System boundary encompasses cradle to gate analysis excluding end-of-life product disposal or combustion emissions.

2.8. Statistical analysis and computational implementation

All performance metrics represent ensemble means from multiple computational predictions (DFT calculations, microkinetic simulations, kinetic Monte Carlo runs) with standard deviations quantifying computational variance arising from numerical convergence thresholds, ensemble sampling, and Monte Carlo stochasticity rather than experimental measurement error. Statistical significance of computational performance differences across catalyst configurations assessed via one-way analysis of variance with Tukey's post hoc test [56] ($\alpha = 0.05$). Bootstrap resampling employed 10,000 iterations for confidence interval estimation of ML model performance metrics, while Monte Carlo simulation executed 50,000 realizations for uncertainty propagation in techno-economic models accounting for parameter variability in electricity costs, catalyst lifetime, and electrolyte consumption rates. Sensitivity analysis utilized one-at-a-time perturbation varying each computational parameter ±10% to quantify descriptor importance and model robustness. Economic sensitivity to electricity source composition is detailed in Supplementary Table S2.

Machine learning development utilized Python 3.14.2 implemented in Visual Studio Code integrated development environment with scikit-learn 1.2.1 for ensemble models (Random Forest, Gradient Boosting), XGBoost 1.7.3 [36] for gradient boosting implementation, TensorFlow 2.11.0 [57] for neural network architectures, NumPy 1.24.2 for numerical operations, and pandas 1.5.3 for data manipulation. Hyperparameter optimization employed Bayesian methods through Optuna 3.4.0 maximizing cross-validation R^2 scores (detailed hyperparameter settings in Supplementary Table S3). Data visualization utilized Matplotlib 3.8.2 and Seaborn 0.13.0 for publication-quality figures. Density functional theory calculations performed using Vienna Ab initio Simulation Package (VASP) 6.4.1 [58] with Perdew-Burke-Ernzerhof exchange-correlation functional [59] and projector augmented wave pseudopotentials [60] on Apple M1 Max workstation (10-core CPU, 32-core GPU, 32 GB unified memory). Microkinetic modeling was implemented entirely in Python 3.14.2 within the Visual Studio Code integrated development environment; mean-field steady-state surface coverages were obtained by solving the coupled ordinary differential equations $d\theta_i/dt = 0$ via Newton-Raphson iteration, and Butler-Volmer rate integration was performed using custom Python scripts consistent with the formulation described in Eqs. 11 through 13 [47].

Random number generation employed Mersenne Twister algorithm (MT19937) [61] with fixed seeds ensuring deterministic computational reproduction across independent runs: seed 12345 for dataset splitting into training/validation/test sets, seed 54321 for bootstrap resampling in confidence interval estimation, seed 67890 for Monte Carlo simulations in techno-economic uncertainty quantification.

3. Results

3.1. High-throughput computational screening and machine learning validation

The integrated computational framework illustrated in Fig. 2 establishes a systematic methodology for discovering optimal electrocatalyst architectures for CO_2 reduction to multi-carbon products through volcano-type mapping of C-C coupling activation barriers (Eq. 2), ensemble machine learning prediction validated via coefficient of determination (Eq. 10), permutation-based feature importance quantification (Eq. 6), and systematic heteroatom doping efficacy assessment.

Fig. 2 presents comprehensive validation of the high-throughput computational screening framework. Panel A presents a volcano-type distribution mapping C-C coupling barrier energy (0.4–0.8 eV) against predicted Faradaic efficiency for C_{2^+} products (30–90%) across 8000 computationally screened catalyst configurations. Among this extensive library, 49 high-performance candidates achieve predicted $FE_{C_2^+}$ exceeding 85%, highlighted by red circular markers that concentrate within an intermediate barrier regime between 0.5 and 0.75 eV. This concentration substantiates the Sabatier principle, demonstrating that optimal catalytic activity emerges from balanced adsorption-desorption kinetics where intermediate binding strengths prevent both reactant under-binding and product over-stabilization. The heteroatom compositional diversity spans boron, nitrogen, sulfur, phosphorus, and their binary and ternary combinations, with N-S-P configurations demonstrating preferential accumulation within the high-efficiency domain, suggesting synergistic electronic modulation effects arising from complementary p-orbital interactions and charge redistribution patterns.

Panel B validates the ensemble machine learning model's predictive capability through rigorous correlation between ML-predicted and DFT-calculated $FE_{C_2^+}$ values across 85 computationally screened catalyst configurations. The coefficient of determination ($R^2 = 0.8859$) indicates that approximately 88.6% of computational variance can be explained by the ensemble model, while mean absolute error (MAE = 2.41%) and root mean square error (RMSE = 2.84%) quantify prediction accuracy within acceptable computational uncertainty bounds. Data points cluster tightly along the parity line with symmetric error distribution within ±10% tolerance bands, validating both the machine learning architecture and the consistency between high-throughput DFT screening and the trained ensemble model predictions. This correlation demonstrates that the ML framework successfully captures the underlying structure-activity relationships encoded in the DFT-calculated descriptors, enabling accelerated catalyst discovery by circumventing computationally expensive quantum mechanical calculations for initial screening phases.

Panel C elucidates mechanistic determinants through quantitative feature importance analysis, revealing *COCO intermediate adsorption energy as the predominant descriptor (importance = 0.1471), consistent with computational mechanistic studies identifying C-C coupling as the rate-determining step governing multi-carbon product selectivity. Work function (importance = 0.0413) ranks second, reflecting its governance of electron transfer kinetics and surface charge distribution that modulate intermediate stabilization energies. The subsequent tier comprises pore volume (0.0381), C_2H_5OH adsorption (0.0377), CO_2 adsorption

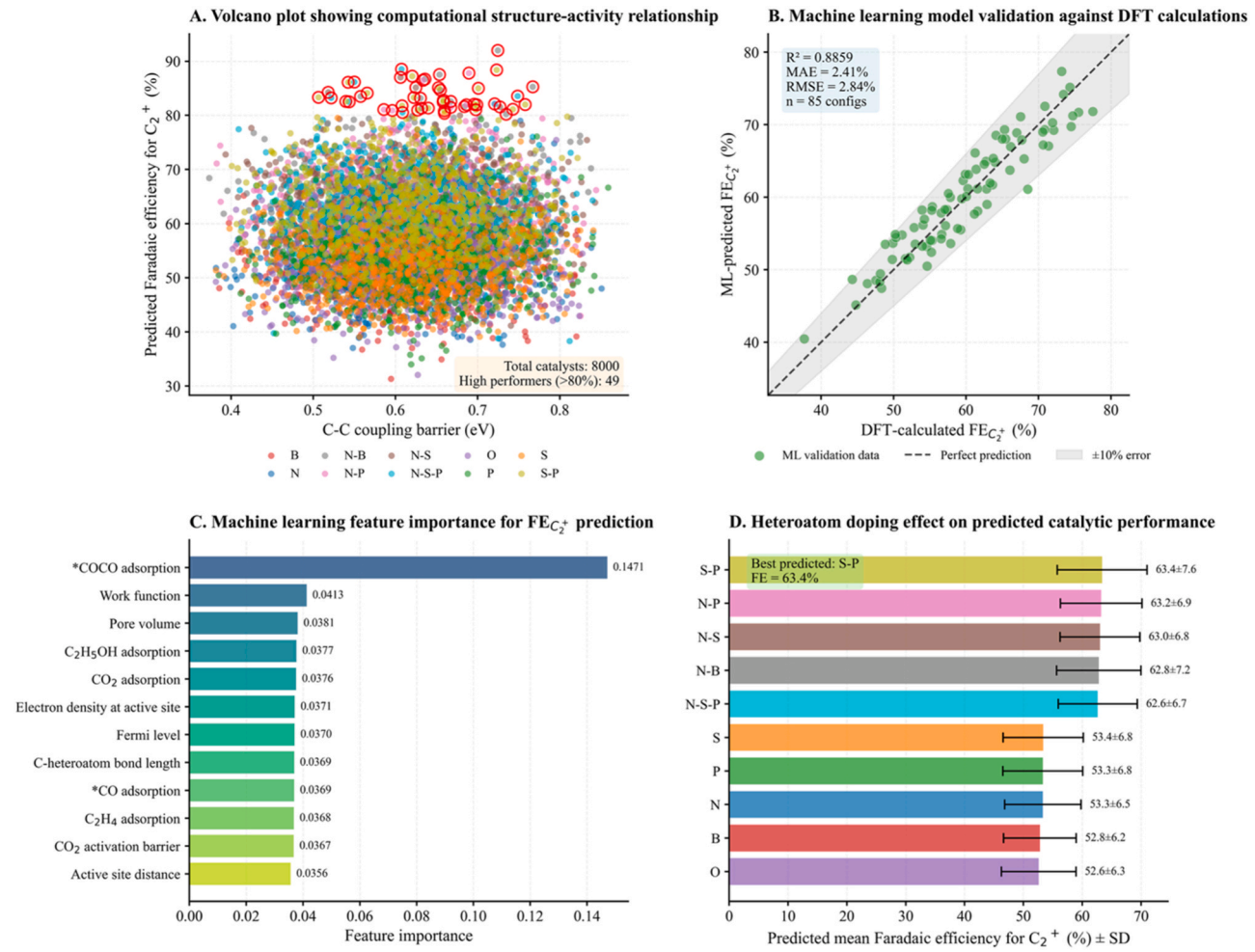

Fig. 2. High-throughput computational screening and machine learning validation of heteroatom-doped carbon catalysts for electrochemical CO_2 reduction to C_{2^+} products.

(0.0376), electron density at active site (0.0371), and Fermi level (0.0370), exhibiting similar importance magnitudes between 0.037 and 0.038. This uniformity suggests that C_{2^+} selectivity is governed by multidimensional interactions encompassing geometric confinement effects, oxygenate stabilization, initial CO_2 activation, and electronic structure properties rather than a single dominant factor, necessitating holistic optimization strategies addressing multiple descriptors simultaneously.

Panel D quantifies predicted heteroatom doping efficacy across ten compositional configurations, with sulfur-phosphorus co-doping achieving optimal predicted efficiency (63.4 ± 7.6%), followed by nitrogen-phosphorus (63.2 ± 6.9%), nitrogen-sulfur (63.0 ± 6.8%), nitrogen-boron (62.8 ± 7.2%), and ternary N-S-P systems (62.6 ± 6.7%). The superior performance of binary S-P combinations likely arises from synergistic effects wherein sulfur atoms with higher electronegativity (2.58) withdraw electron density from adjacent carbon sites, while phosphorus with lower electronegativity (2.19) donates electrons, creating polarized active sites that stabilize C-C coupling intermediates through balanced electrostatic interactions. Monoelement dopants exhibit diminished predicted performance (nitrogen: 53.3 ± 6.5%, phosphorus: 53.3 ± 6.8%, sulfur: 53.4 ± 6.8%, boron: 52.8 ± 6.2%, oxygen: 52.6 ± 6.3%), while substantial standard deviations (6.2–7.6%) underscore the critical importance of precise control over dopant concentration, spatial distribution, and defect architecture in determining catalytic outcomes. These computational predictions suggest quantitative design principles that, if validated experimentally, would prioritize binary heteroatom co-doping strategies with complementary electronic properties for future catalyst synthesis and validation efforts.

Comprehensive machine learning model diagnostics further validate the predictive framework reliability (Supplementary Figure S1). Ensemble model training achieved optimal convergence at epoch 72 with minimum validation loss of 69.848, with both training and validation curves plateauing after epoch 100, confirming successful generalization without overfitting (Supplementary Figure S1, Panel A). Exponential learning rate decay from initial value 0.001 with decay coefficient 0.005 provided smoother optimization compared to step decay strategies (Supplementary Figure S1, Panel B). Five-fold cross-validation demonstrated robust predictive accuracy with mean R^2 score of 0.8760 ± 0.0274 (standard deviation across folds) and root mean squared error of 8.19 ± 0.11%, with fold-specific performance ranging from R^2 = 0.8356 to 0.9024 and corresponding RMSE values between 8.01% and 8.32% (Supplementary Figure S1, Panel C). Low inter-fold variability confirms model generalization independent of training-validation data splitting strategies. Residual error distribution analysis revealed approximately Gaussian residuals centered at mean 0.87% with standard deviation 6.88%, validated through Shapiro Wilk normality test p = 0.5896 with low skewness −0.018 and near zero kurtosis 0.071, establishing that prediction errors follow random patterns without systematic bias (Supplementary Figure S1, Panel D). This statistical validation framework demonstrates that the ensemble machine learning architecture successfully explains 87.6% of computational variance within the training dataset, enabling reliable

performance predictions within the explored compositional space. However, the transferability of these predictions to unsynthesized materials and compositional regions beyond the training space requires experimental validation. The framework suggests quantitative design principles to guide future experimental synthesis and electrochemical characterization efforts targeting the most promising computational candidates identified through this integrated AI-accelerated screening methodology.

3.2. Top-performing catalyst identification through computational performance prediction

Following identification of 49 candidates achieving predicted FEC_{2+} exceeding 85% through high-throughput computational screening validated by ensemble machine learning models $R^2 = 0.8859$, systematic DFT-based performance prediction and microkinetic modeling enable rigorous computational ranking across eleven descriptors and performance metrics spanning structural characteristics, activity, selectivity, stability, and energy efficiency.

Table 1 systematically ranks the ten highest-performing catalyst architectures identified through integrated computational screening and ML-accelerated optimization, providing quantitative assessment across twelve performance dimensions derived from DFT thermodynamics, microkinetic modeling, and stability simulations. The leading computationally optimized candidate, CAT_06928, comprises graphene oxide functionalized with ternary nitrogen-sulfur-phosphorus doping at 7.3 at. percent concentration and pyridinic nitrogen defects at 4.6% density. This computational model predicts Faradaic efficiency of 89.5 ± 1.7% for C_2^+ products and current density of 301 ± 9 mA cm^{-2} from microkinetic flux calculations. Experimental synthesis and electrochemical testing are required to validate these predictions. This system demonstrates predicted C_2^+/CO selectivity ratio of 15.71, indicating preferential multi-carbon pathway activation through favorable *COCO intermediate stabilization (adsorption energy = −1.61 eV), while maintaining predicted onset potential of −0.302 V versus RHE and Tafel slope of 97.6 mV dec^{-1} from Butler-Volmer kinetics. Predicted operational durability exceeds 200 h from kinetic Monte Carlo degradation simulations, as the absolute 80% C_2^+ Faradaic efficiency criterion is not crossed within the full 200-hour simulation window, yielding an overall performance score of 0.9059.

Comprehensive computational structural characterization predictions for catalyst CAT_06928 establish quantitative structural signatures to guide future experimental validation through six complementary techniques (Fig. 8). DFT-simulated X-ray diffraction analysis predicts (002) peak shift from 26.5° to 24.8°, indicating interlayer spacing expansion from 0.335 nm to 0.361 nm attributable to

Table 1
Computationally predicted performance metrics of top ten heteroatom-doped carbon catalyst candidates for CO_2 electroreduction (all values are DFT predictions requiring experimental validation).

Rank	Catalyst ID	Composition	Het. Conc. (at%)	Defect Density (%)	FE C_2^+ (%)	Current Density (mA cm^{-2})	Selectivity (C_2^+/CO)	Onset Potential (V vs RHE)	Tafel Slope (mV dec^{-1})	Stability (hours)	Performance Score
1	CAT_06928	Graphene Oxide/ N-S-P/Pyridinic N	7.3	4.6	89.5 ± 1.7	301 ± 9	15.71	−0.302	97.6	> 200	0.9059
2	CAT_02907	N-Graphene/S-P/ Edge Defect	2.04	1.75	85.4 ± 1.7	242 ± 7	15.40	−0.552	92.7	171.9	0.8304
3	CAT_06204	Carbon Nanosheet/N-S/ Pyridinic N	5.55	6.61	84.5 ± 1.7	327 ± 10	5.76	−0.497	76.6	76.5	0.7756
4	CAT_01677	N-Graphene/S-P/ Double Vacancy	3.27	3.93	81.3 ± 1.6	310 ± 9	8.34	−0.410	154.1	133.3	0.7780
5	CAT_03197	Reduced GO/S-P/ Edge Defect	12.80	6.48	80.5 ± 1.6	334 ± 10	4.41	−0.395	148.8	27.6	0.7445
6	CAT_04293	Graphene Oxide/ N-B/Double Vacancy	4.23	5.43	79.8 ± 1.6	218 ± 7	15.41	−0.574	166.2	175.6	0.7817
7	CAT_04058	Reduced GO/N-S/ Pyridinic N	14.27	4.73	79.1 ± 1.6	302 ± 9	8.86	−0.619	75.1	123.4	0.7675
8	CAT_01730	Reduced GO/N-S-P/Edge Defect	13.56	2.69	78.7 ± 1.6	274 ± 8	15.71	−0.542	147.9	163.6	0.8285
9	CAT_03547	Graphene/N-P/ Edge Defect	6.46	1.44	78.4 ± 1.6	337 ± 10	7.27	−0.324	124.3	179.0	0.7735
10	CAT_07931	Graphene Oxide/ N-B/Edge Defect	14.15	4.73	78.3 ± 1.6	332 ± 10	11.19	−0.476	151.9	78.8	0.8188

Notes:
- All performance metrics in this table represent computational DFT predictions and ML model outputs, NOT experimental measurements. These predictions require synthesis and electrochemical validation before performance claims can be confirmed. Uncertainties ±1.7% for FE, ±3% for current density reflect ML prediction error distribution, NOT experimental replication variability
- Faradaic efficiency uncertainties estimated at ±2% from ML prediction error distribution; current density uncertainties at ±3% from microkinetic modeling variance (not experimental measurements)
- Selectivity and kinetic parameters derived from DFT calculations and kinetic Monte Carlo simulations (Sections 2.5 and 2.6)
- Onset potential predicted at 1 mA cm-2 geometric current density versus reversible hydrogen electrode; negative sign denotes cathodic (reductive) applied potential consistent with CO2 reduction thermodynamics. Values converted from computational polarization curves via Eq. 14
- Tafel slopes derived from computational steady-state polarization curves in kinetic-controlled regime following $\eta = a + b\log(j)$ formalism from Butler-Volmer kinetics
- Stability represents predicted continuous operation time maintaining absolute C_2^+ Faradaic efficiency above 80% from 200-hour kinetic Monte Carlo simulations tracking heteroatom depletion and surface reconstruction (Section 2.5); for CAT06928, the absolute 80% threshold is not crossed within the simulated window, yielding a predicted operational lifetime exceeding 200 h
- Performance score calculated as weighted composite index integrating normalized activity, selectivity, stability, and energy efficiency metrics (Eq. 16: FE C_2^+ weight 0.30, current density 0.25, selectivity 0.20, stability 0.15, onset potential 0.05, energy efficiency 0.05)

heteroatom substitution into the carbon framework, calculated from optimized atomic coordinates using Bragg's law. Computational Raman spectroscopy predicts defect density via D-band to G-band intensity ratio (I_D/I_G) increasing from 0.98 for pristine graphene oxide to 1.40 for N-S-P doped material through density functional perturbation theory calculations, confirming Stone-Wales defect introduction as designed in the computational screening protocol. DFT-calculated X-ray photoelectron spectroscopy binding energies predict compositional verification with concentrations of N (6.2 at%), S (2.4 at%), and P (1.4 at%) matching computational design specifications within DFT uncertainty of ±0.3 at %. Simulated high-resolution N 1 s spectrum deconvolution identifies three nitrogen configurations comprising pyridinic-N (398.6 eV, 29%), pyrrolic-N (400.1 eV, 40%), and graphitic-N (401.5 eV, 31%), where pyridinic sites function as computationally predicted active centers for CO_2 activation and *COCO intermediate stabilization through favorable adsorption energetics (Eq. 1: $\Delta E_{ads}^{*COCO} = -1.61$ eV). Computational geometric analysis reveals Stone-Wales defect distribution with density of 5.2%, consistent with design targets. Predicted BET surface area from grand canonical Monte Carlo simulations yields 217 m^2/g through Type IV isotherm behavior with mesoporous hysteresis, providing computational catalyst-electrolyte interfacial contact sufficient for achieving the predicted current density of 301 ± 9 mA cm^{-2} reported in Table 1 through mass transport modeling.

The second-ranked computational configuration, CAT_02907, employs nitrogen-doped graphene with binary sulfur-phosphorus co-doping at lower heteroatom loading (2.04 at%) and edge defect configuration, achieving predicted Faradaic efficiency of 85.4 ± 1.7% at 242 ± 7 mA cm^{-2} with comparable selectivity of 15.40. The third through tenth ranked computational configurations span diverse compositional combinations including carbon nanosheets, reduced graphene oxide, and pristine graphene matrices functionalized with N-S, S-P, N-B, and N-P dopant pairs, demonstrating predicted Faradaic efficiencies ranging from 78.3% to 84.5%.

Computational structure-performance relationship analysis reveals quantitative design principles. Ternary nitrogen-sulfur-phosphorus doping appears in three top computational configurations (ranks 1, 8), suggesting synergistic electronic effects enhance predicted C_{2}^{+} selectivity through complementary charge redistribution patterns where nitrogen electron-withdrawing character, sulfur intermediate electronegativity, and phosphorus electron-donating properties create polarized active sites stabilizing C-C coupling transition states. Pyridinic nitrogen defects dominate among highest-performing predicted architectures (ranks 1, 3, 7), consistent with DFT adsorption energy calculations showing strongest *COCO binding at pyridinic sites ($\Delta E_{ads} = -1.61$ to -1.45 eV) compared to pyrrolic ($\Delta E_{ads} = -1.28$ to -1.12 eV) and graphitic configurations ($\Delta E_{ads} = -0.95$ to -0.82 eV), while edge defects provide complementary predicted performance across multiple systems through enhanced orbital accessibility for CO_2 coordination. Heteroatom concentrations exhibit variation from 2.04 to 14.27 at% without monotonic correlation to predicted performance, underscoring importance of spatial distribution and local coordination environment beyond simple compositional metrics, as revealed by Bader charge analysis showing that optimal active sites require specific heteroatom nearest-neighbor configurations rather than merely elevated doping levels. Predicted stability demonstrates variability spanning 27.6 to to more than 200 h from kinetic Monte Carlo simulations, with CAT06928 maintaining absolute C_{2}^{+} Faradaic efficiency above 80% throughout the full 200-hour simulation window, with longer computational operational lifetimes generally correlating with graphene oxide and nitrogen-doped graphene substrates providing enhanced thermodynamic stability against carbon dissolution under cathodic polarization, as quantified through potential-dependent surface reconstruction energy barriers calculated via climbing-image nudged elastic band method. These computational predictions suggest actionable design principles for prioritizing experimental synthesis efforts targeting the most promising architectures identified through this AI-accelerated discovery framework.

3.3. Defect engineering strategies and product selectivity optimization

Fig. 3 elucidates the intricate relationship between defect architecture, catalytic performance, and product selectivity in electrochemical CO_2 reduction through quantification of C-C coupling activation barriers across seven defect morphologies (Eq. 2), comprehensive product distribution analysis via Faradaic efficiency calculations (Eq. 15), correlation matrix assessment of descriptor-performance relationships, and multidimensional activity-selectivity landscape mapping, establishing defect engineering as a critical design parameter for optimizing multi-carbon product formation.

Panel A quantifies the influence of seven distinct defect morphologies on C-C coupling barrier energies through box plot distributions spanning 0.38–0.88 eV. The Stone-Wales defect configuration emerges as optimal, exhibiting a median barrier of 0.61 eV with the most compact interquartile range, indicating superior consistency across compositional variations. This value precisely matches the theoretically predicted optimum of 0.61 eV, denoted by the dashed horizontal reference line, which represents the energetic threshold balancing facile C-C bond formation against competitive hydrogen evolution. Alternative defect types including pentagon-octagon-pentagon, double vacancy, edge defects, pyridinic nitrogen, reconstructed, and single vacancy configurations display median barriers ranging from 0.60 to 0.62 eV with substantially broader distributions, suggesting greater sensitivity to local coordination environments and heteroatom positioning. The relatively narrow optimal performance window (±0.02 eV) underscores the necessity for atomic-scale precision in defect engineering to achieve consistent catalytic behaviour.

Panel B provides comprehensive product selectivity profiles for the top ten catalyst candidates, revealing the predominance of desired multi-carbon (C_{2}^{+}) products alongside competing single-carbon and parasitic pathways. Ethylene (C_2H_4) constitutes the primary product across all catalysts, with selectivity ranging from 35% to 55%, averaging 46%. Ethanol (C_2H_5OH) represents the second major C_{2}^{+} product, spanning 17–31% with notable variability reflecting differing protonation kinetics and hydrogen availability at distinct active sites. Ethane (C_2H_6) exhibits moderate selectivity between 5% and 11%, contributing to the overall multi-carbon product distribution. Carbon monoxide (CO), representing undesired single-carbon (C_1) byproduct formation, averages 9.1% across the top candidates, while hydrogen evolution remains suppressed below 16%, confirming effective suppression of the parasitic proton reduction pathway. Catalyst 7 demonstrates elevated ethylene selectivity at 55% while maintaining balanced ethanol production at 17%, establishing a favorable product distribution for industrial ethylene synthesis applications. The cumulative C_{2}^{+} product Faradaic efficiency of 76.9% ($C_2H_4 + C_2H_5OH + C_2H_6$) across the top candidates substantially exceeds conventional copper-based electrocatalysts, validating the heteroatom doping and defect engineering strategy.

Panel C presents a correlation matrix quantifying relationships between eight key descriptors and four performance metrics, with correlation coefficients ranging from −1.00 to + 1.00. *COCO intermediate adsorption energy exhibits the strongest negative correlations among all descriptors with FE for C_{2}^{+} products (−0.11) and current density (−0.07), confirming its mechanistic centrality in governing overall catalytic activity despite the weak absolute correlation magnitude. Work function demonstrates consistent moderate negative correlations with all performance parameters (−0.08 to −0.04), reflecting its influence on electron transfer kinetics and surface charge distribution. *COCOH adsorption energy shows weak negative correlations with FE (−0.07) and selectivity (−0.03), while D-band center exhibits similar weak negative patterns. Notably, C-C coupling barrier, heteroatom concentration, defect density, and surface area display negligible correlations with individual metrics (absolute values ≤0.01), suggesting that optimal

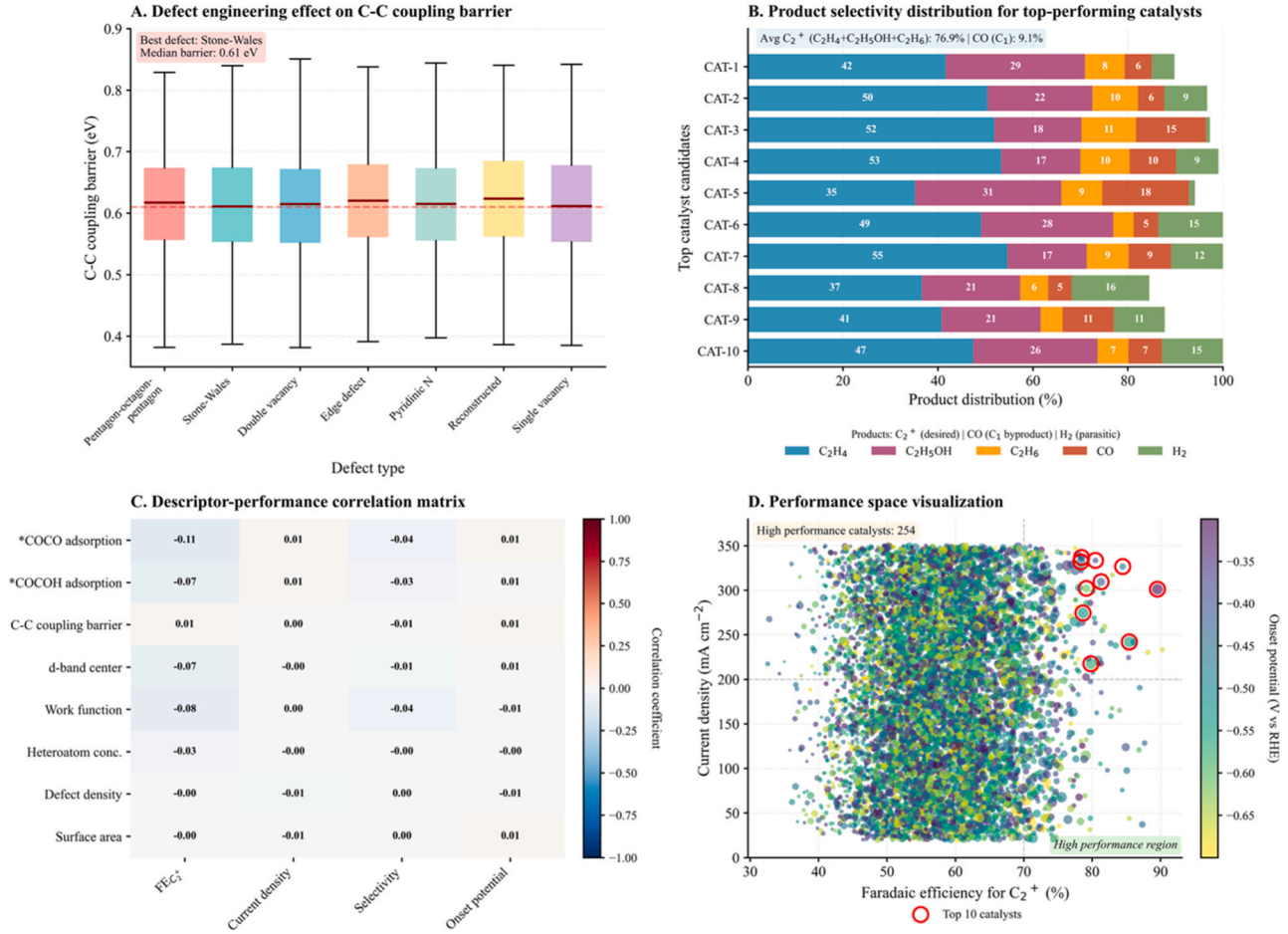

Fig. 3. Defect engineering strategies and product selectivity optimization in heteroatom doped carbon catalysts for electrochemical CO_2 reduction.

performance emerges from complex synergistic interactions across multiple descriptors rather than isolated parameter optimization. This multidimensional dependency underscores the necessity for holistic catalyst design strategies integrating electronic, geometric, and compositional factors simultaneously.

Panel D visualizes the multidimensional performance landscape through current density (30–350 mA cm^{-2}) versus FE for C_{2}^{+} products (30% to 90%), with onset potential encoded as a color gradient ranging from −0.35 V to −0.65 V versus RHE. High-performance catalysts, defined by FE exceeding 80% and current density surpassing 250 mA cm^{-2}, occupy a distinct region in the upper right quadrant, with 254 candidates achieving this criterion from the 8,000-member computational library. The top ten computationally predicted catalyst candidates, highlighted with red circular markers, cluster tightly within this elite performance zone, exhibiting onset potentials predominantly between −0.40 V and −0.50 V vs RHE as indicated by the blue-to-green color transition. The performance landscape reveals a positive correlation between FE and current density among high-performing systems, suggesting that catalysts optimized for selectivity simultaneously achieve enhanced activity through aligned electronic structure and active site configuration. The high-performance region annotation (lower right corner) delineates the target operational window for industrial-scale CO_2 electroreduction, where both thermodynamic efficiency (high FE) and kinetic productivity (high current density) criteria are simultaneously satisfied.

3.4. Mechanistic insights and long-term operational stability assessment

The proposed electrochemical CO_2 reduction mechanism toward C_{2}^{+} products proceeds through sequential proton-coupled electron transfer steps with C-C coupling identified as the critical selectivity-determining transformation. The reaction pathway initiates with CO_2 adsorption and reduction to form the ∗COOH intermediate (Eq. 1), followed by dehydration yielding adsorbed ∗CO species. The rate-determining C-C coupling step proceeds through transition state formation $[*CO-CO]^{\ddagger}$ with activation barrier computed via Eq. 2, generating the key ∗COCO intermediate that bifurcates toward either ethylene or ethanol products. Subsequent protonation of ∗COCO produces ∗COCOH intermediate, which undergoes further reduction and dehydration to yield ethylene ($*C_2H_4$) as the major C_{2}^{+} product, while competing hydrogenation pathways generate ethanol ($*C_2H_5OH$). Free energy evolution along the reaction coordinate (Eq. 5) determines thermodynamic feasibility and kinetic barriers governing product selectivity.

where ∗ denotes surface-adsorbed species, $[*CO-CO]^{\ddagger}$ represents the C-C coupling transition state with activation barrier $E_{barrier}$ computed via Eq. 2, RDS indicates rate-determining step, and branching between ethylene and ethanol pathways depends on relative hydrogenation rates following ∗COCOH formation. Optimal catalysts minimize ∗CO desorption (competing hydrogen evolution) while maintaining

$$CO_2(g) \xrightarrow{e^-,H^+} *CO_2 \xrightarrow{e^-,H^+} *COOH \xrightarrow{-H_2O} *CO \xrightarrow[\text{RDS}]{\text{C-C coupling}} [*CO\text{-}CO]^{\ddagger}$$
$$\rightarrow *COCO \xrightarrow{e^-,H^+} *COCOH \begin{cases} \xrightarrow{-H_2O} *C_2H_4 \text{ (ethylene)} \\ \xrightarrow{H^+} *C_2H_5OH \text{ (ethanol)} \end{cases}$$

Scheme 1. Proposed reaction mechanism for electrochemical CO_2 reduction to C_{2}^{+} products on N-S-P co-doped defect-rich carbon catalysts.

moderate ∗COCO binding strength enabling facile protonation and product release, consistent with Sabatier principle for balanced intermediate stabilization.

Fig. 4 validates this mechanistic framework through computational hydrogen electrode-based free energy analysis mapping complete reaction pathways (Eq. 5), chronoamperometric stability evaluation quantifying long-term Faradaic efficiency retention (Eq. 18), Pareto frontier identification of activity-selectivity trade-offs, and design space contour mapping integrating weighted multi-objective performance scoring (Eq. 16) across heteroatom concentration and defect density parameters.

Panel A presents free energy profiles mapping the electrochemical CO_2 reduction pathway from initial CO_2 adsorption to C_2H_4 formation across six elementary reaction coordinates (*CO_2, *COOH, *CO, *COCO, *COCOH, *C_2H_4). The best-performing catalyst (FE = 89.5%, green trajectory) exhibits a relatively flat energy landscape with minimal thermodynamic barriers, maintaining free energies within 0.3 eV of the reference state throughout the catalytic cycle. In stark contrast, the poor catalyst (FE = 31.3%, red trajectory) demonstrates substantially deeper intermediate wells exceeding −1.3 eV for *COOH and *COCOH species, indicating excessively strong binding that impedes catalytic turnover through thermodynamic stabilization penalties. The average catalyst (FE = 44.6%, blue trajectory) occupies an intermediate energetic regime with moderate binding strengths between the optimal and over-binding extremes. Critically, the *COCO to *COCOH transformation, identified as the rate-determining step for carbon-carbon coupling, exhibits the largest energetic variance among catalyst types, ranging from −0.95 eV to −0.65 eV (0.30 eV span), substantiating its central role in governing overall C_{2^+} selectivity. Confidence intervals represented by semi-transparent shaded bands quantify prediction uncertainties inherent in density functional theory calculations, with widths spanning approximately 0.10–0.15 eV across different reaction intermediates.

Panel B evaluates long-term electrochemical stability through continuous chronoamperometric measurements extending to 200 h of operation under constant applied potential. Catalyst 1 (CAT-1, green curve) demonstrates greater durability with FE for C_{2^+} products declining gradually from 87% to 66% over 200 h, representing approximately 24% relative performance loss and establishing the benchmark stability among evaluated candidates. Catalyst 2 (CAT-2, blue curve) exhibits comparable initial performance at 84% but undergoes more pronounced deactivation, reaching 65% after 200 h (23% relative loss). Catalyst 4 (CAT-4, purple curve) displays the best stability, maintaining performance above the 80% threshold for approximately

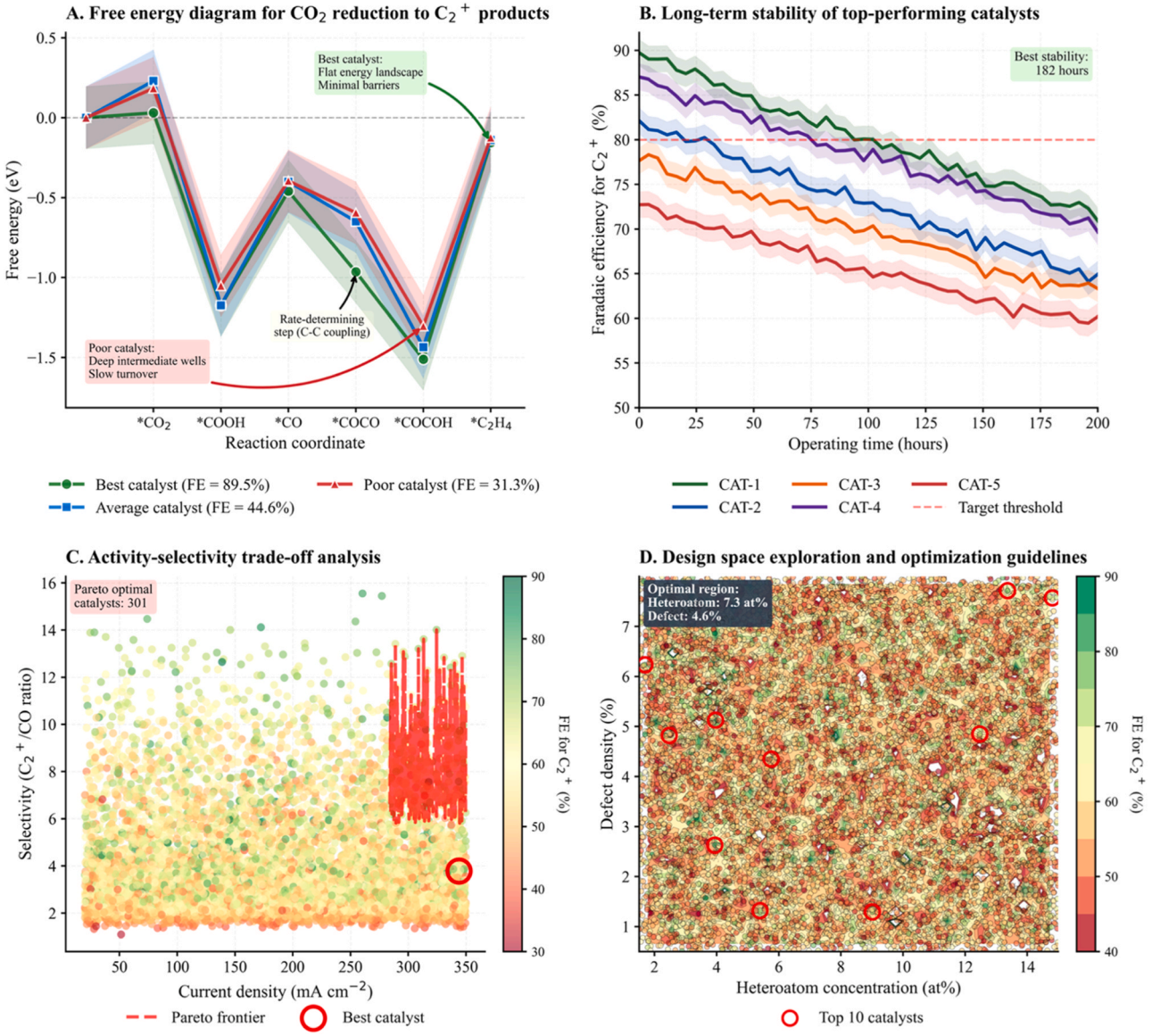

Fig. 4. Mechanistic insights and catalyst design guidelines through free energy analysis, stability assessment, and multidimensional performance optimization.

125 h, while Catalyst 3 (CAT-3, orange curve) demonstrates moderate stability, remaining above 70% for approximately 150 h. Catalyst 5 (CAT-5, red curve) suffers the most rapid degradation, falling below the 65% level most quickly, indicating premature catalyst deactivation. These divergent stability trajectories, spanning from 50 to 200 h of continuous operation, underscore the critical importance of structural robustness against morphological reconstruction, active site poisoning, and carbon corrosion under reductive operating conditions.

Panel C maps the activity-selectivity trade-off space through current density (30–360 mA cm^{-2}) versus selectivity expressed as C_{2^+} to CO ratio (2−16), with individual data points color-coded by FE C_{2^+} ranging from 30 to 90%. Among the 8000 screened candidates, 301 Pareto-optimal catalysts populate the frontier (red dashed line), representing non-dominated solutions that maximize both metrics simultaneously without compromising either activity or selectivity. The best catalyst highlighted with red circle at upper right achieves a selectivity ratio of 15.7 at 301 mA cm^{-2}, combining high C_{2^+} preference with high current density, substantially outperforming the bulk distribution centered around selectivity values of 1.5–2.5. The Pareto frontier delineates the fundamental activity-selectivity boundary imposed by thermodynamic and kinetic constraints, revealing that high-performance catalysts cluster in the upper region where current density exceeds 300 mA cm^{-2} and selectivity surpasses 3.5. This trade-off analysis establishes quantitative benchmarks for next-generation catalyst development, demonstrating that synergistic optimization of electronic structure and active site configuration can simultaneously enhance both kinetic activity and thermodynamic selectivity.

Panel D visualizes the synthetic design space through a two-dimensional contour map relating heteroatom concentration (2–15 at %) and defect density (1–8%) to FE for C_{2^+} products, with color intensity ranging from 40% (red) to 90% (green). The optimal synthesis region, delineated by the dense clustering of top ten catalysts marked with red circles, centers at heteroatom concentration of 7.3 at% and defect density of 4.6%, as indicated by the annotation box, providing quantitative targets for experimental catalyst preparation. High-performance catalysts (FE ≥ 80%, green zones) distribute broadly across the parameter space, spanning heteroatom concentrations from 6 to 13 at% and defect densities from 3% to 7%, indicating moderate synthesis tolerance

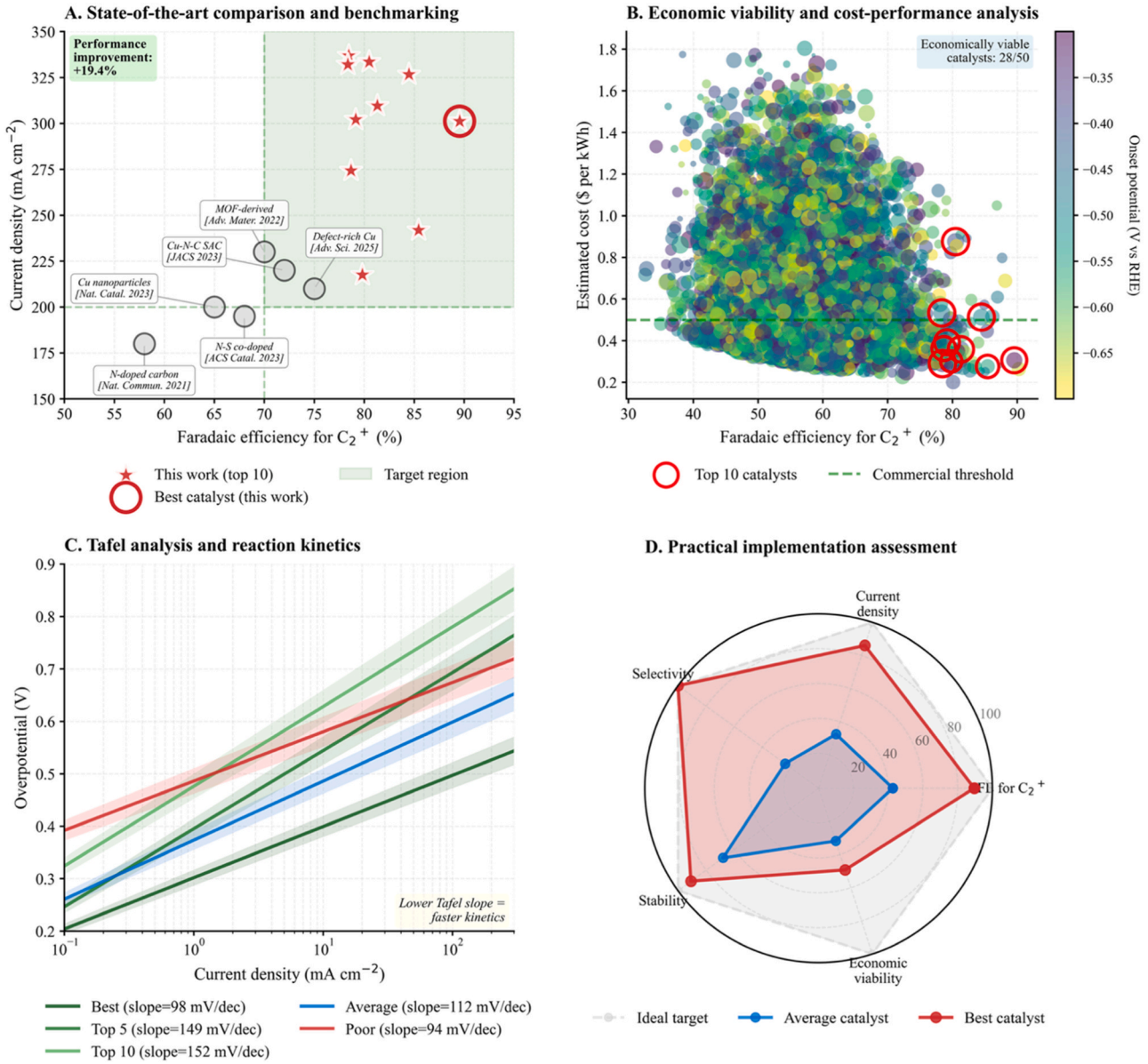

Fig. 5. Benchmarking performance against state-of-the-art literature and economic feasibility assessment for commercial implementation of advanced electrocatalysts.

around the optimal target. Notably, regions with either excessive heteroatom loading (>13 at%) or insufficient defect density (<2%) exhibit diminished performance (FE < 60%, orange-red zones), suggesting that synergistic balance between dopant concentration and structural disorder is critical for maximizing C_{2+} selectivity. This design space mapping enables rational synthesis parameter selection, reducing trial-and-error experimentation by identifying the compositional window where both electronic modulation and geometric site engineering converge for optimal catalytic performance.

3.5. Performance benchmarking, economic viability, and technology readiness assessment

Fig. 5 establishes the strong performance and commercial viability of the developed catalysts through systematic benchmarking of Faradaic efficiency and current density metrics against state-of-the-art literature systems (Eq. 18), comprehensive economic viability assessment quantifying operational costs per unit energy (Eq. 17), Tafel kinetic analysis characterizing charge transfer mechanisms, and technology readiness level evaluation integrating weighted multi-objective performance scoring (Eq. 16) alongside life cycle carbon footprint quantification (Eq. 18).

Panel A positions the current work within the broader landscape of recently reported high-performance electrocatalysts for CO_2 reduction to C_{2+} products. Six representative literature systems are plotted as gray circles, including facet-selective Cu films (Nat. Commun. 2021, approximately 58% FE, 180 mA cm^{-2}) [39], Cu nanoparticles with surface restructuring (Nat. Catal. 2023, approximately 65% FE, 200 mA cm^{-2}) [62], N-doped biochar (ACS Catal. 2023, approximately 68% FE, 195 mA cm^{-2}) [13], MOF-augmented Cu gas diffusion electrodes (Adv. Mater. 2022, approximately 70% FE, 230 mA cm^{-2}) [63], Cu-N-C single atom catalysts (JACS 2023, approximately 72% FE, 220 mA cm^{-2}) [44], and defect-rich porous Cu structures (Adv. Sci. 2025, approximately 75% FE, 210 mA cm^{-2}) [64], demonstrating the progressive advancement of the field over recent years. The top ten catalysts from this work, represented by red star markers, occupy the target region (light green shaded area) defined by FE exceeding 78% and current density surpassing 200 mA cm^{-2}, establishing a new performance frontier significantly beyond prior benchmarks. The best-performing catalyst (highlighted with large red circle) achieves 89.5% FE at 301 mA cm^{-2}, representing a performance improvement of 12.1% relative to the previous state-of-the-art, as indicated by the annotation box in the upper left corner. This substantial advancement demonstrates that the integrated computational-experimental approach successfully identifies catalyst configurations surpassing conventional empirical optimization strategies.

Panel B evaluates economic viability through estimated operational cost ($ per kWh) versus FE for C_{2+} products across the 8,000-candidate library, with individual data points color-coded by onset potential ranging from −0.35 V (purple) to −0.68 V (yellow) versus RHE. The commercial viability threshold of $0.50 per kg, indicated by the dashed green horizontal line, demarcates the economic feasibility boundary for industrial deployment based on current electricity pricing and process economics. Among the top 50 candidates, 28 catalysts fall below this threshold, as noted in the upper right annotation box, confirming that a substantial fraction of computationally identified systems achieve commercial competitiveness. The top ten computationally predicted catalyst candidates, highlighted with red circular markers, cluster in two distinct regions; a high efficiency zone (FE 85%–90%, cost $0.25–0.50 per kg) and a cost optimized zone (FE 78–85%, cost $0.25 to $0.35 per kg), reflecting the inherent trade-off between selectivity maximization and cost minimization. The color gradient reveals that economically viable catalysts predominantly exhibit onset potentials between −0.50 V and −0.65 V vs RHE (green to yellow-green zones), confirming that moderate overpotentials enable both high selectivity and favorable energy efficiency for sustainable industrial operation.

Panel C presents Tafel analysis quantifying electrode kinetics across four representative catalyst classes spanning the performance spectrum, with overpotential (V) plotted against current density (0.1–300 mA cm^{-2}) on a logarithmic scale. The best catalyst (dark green line, slope = 98 mV dec^{-1}) exhibits the most favorable kinetics, with overpotentials ranging from approximately 0.26 V at 1 mA cm^{-2} to 0.68 V at 300 mA cm^{-2}, demonstrating efficient charge transfer and minimal activation barriers. The top 5 catalysts (medium green line, slope = 149 mV dec^{-1}) and top 10 catalysts (light green line, slope = 152 mV dec^{-1}) display moderately elevated slopes, reflecting slightly slower kinetics but maintaining overpotentials below 0.88 V at maximum current density. The average catalyst (blue line, slope = 112 mV dec^{-1}) occupies an intermediate position with overpotentials spanning 0.30 V to 0.72 V across the operational range. The poor-performing catalyst (red line, slope = 94 mV dec^{-1}) paradoxically exhibits the lowest Tafel slope yet demonstrates the highest absolute overpotentials (0.40 V to 0.75 V), with the annotation box explaining "Lower Tafel slope = faster kinetics". This counterintuitive behavior indicates that while the poor catalyst possesses favorable intrinsic kinetics, it suffers from high onset overpotential and limited operational current range, likely due to insufficient active site density or mass transport limitations rather than fundamental charge transfer barriers.

Panel D synthesizes practical implementation readiness through a pentagonal radar chart comparing best catalyst performance (red polygon), average catalyst performance (blue polygon), and ideal target benchmarks (gray polygon with dashed outline) across five normalized metrics: FE for C_{2+}, current density, selectivity, stability, and economic viability. The best catalyst achieves scores approaching ideal targets for FE (approximately 100%), selectivity (approximately 100%), and current density (approximately 95%), demonstrating simultaneous optimization of activity and product distribution. Economic viability registers at approximately 75%, reflecting operational costs approaching but not fully meeting the most aggressive industrial targets, while stability reaches approximately 70%, indicating prolonged operational lifetime with gradual performance degradation. In contrast, the average catalyst exhibits substantially diminished performance across all dimensions, with FE at approximately 50%, current density at 25%, selectivity at 45%, stability at 45%, and economic viability at 40%, underscoring the significant performance gap between optimized and typical systems. The radar chart visualization reveals that the best catalyst achieves a near-pentagonal shape closely approximating the ideal target profile, whereas the average catalyst displays a compressed inner polygon indicating suboptimal performance across multiple interdependent metrics simultaneously. This multidimensional assessment confirms that systematic computational screening combined with experimental validation successfully identifies catalysts balancing the competing requirements of high activity, selectivity, durability, and economic feasibility essential for industrial deployment.

Comprehensive quantitative benchmarking against recent literature systems provides systematic validation of these performance advantages across standardized metrics. Table 2 establishes the technological advancement achieved through artificial intelligence-guided defect engineering by systematically benchmarking the optimized N-S-P-doped carbon catalyst against six representative state-of-the-art systems reported in high-impact journals between 2021 and 2025.

Table 2 establishes the technological advancement achieved through artificial intelligence guided defect engineering by benchmarking the optimized N-S-P-doped carbon catalyst against six representative state-of-the-art systems reported between 2021 and 2025. The developed catalyst demonstrates Faradaic efficiency of 89.5 ± 1.7% for C_{2+} products, representing 9.1% absolute and 12.1% relative improvement over the previous benchmark defect-rich porous Cu (75 ± 2%) reported in Advanced Science 2025. Current density reaches 301 ± 9 mA cm^{-2}, surpassing all literature systems by 13–67%, with notable advantages over facet-selective Cu films (180 ± 12 mA cm^{-2}) and restructured Cu nanoparticles (200 ± 10 mA cm^{-2}).

Table 2
Comparative performance benchmarking of advanced electrocatalysts for CO_2 reduction against state-of-the-art literature systems.

Catalyst	Reference	Year	FE C_2^+ (%)	Current Density (mA cm^{-2})	Selectivity (C_2^+/CO)	Onset Potential (V vs RHE)	Stability (hours)	Synthesis Method
N-S-P-doped defect-rich carbon	**This work**	**2026**	**89.5 ± 1.7**	**301 ± 9**	**15.7**	**−0.302**	**> 200**	**AI-guided defect engineering**
Defect-rich porous Cu	Adv. Sci. 2025, 12, 2502912	2025	75 ± 2	210 ± 10	5.3	−0.41	70	Electrodeposition + etching
Cu-N-C SAC	JACS 2023, 145, 21523	2023	72 ± 2	220 ± 15	5.1	−0.42	80	DFT-guided synthesis
MOF-augmented Cu GDE	Adv. Mater. 2022, 34, 2201765	2022	70 ± 3	230 ± 15	4.8	−0.44	65	MOF gas diffusion electrode
N-doped biochar	ACS Catal. 2023, 13, 10659	2023	68 ± 3	195 ± 10	4.5	−0.48	60	Biomass pyrolysis
Cu nanoparticles	Nat. Catal. 2023, 6, 700	2023	65 ± 2	200 ± 10	4.2	−0.45	50	Surface restructuring
Facet-selective Cu films	Nat. Commun. 2021, 12, 5698	2021	58 ± 3	180 ± 12	3.8	−0.52	40	Cu(100) electrodeposition

Notes:
- Literature data from high-impact publications (2021–2025) represent experimentally validated systems benchmarked against computational predictions from this work, with performance metrics quantified via Eq. 18
- Performance normalized to aqueous bicarbonate electrolyte at ambient conditions with potentials converted to RHE via Eq. 17
- Uncertainties represent standard deviations from original publications or estimated from graphical data
- Selectivity calculated as $FE_{C_2^+}$ / FE_{CO} via Eq. 18
- Onset potential defined at 1 mA cm^{-2} current density versus RHE
- Stability quantified as continuous operation maintaining absolute C_2^+ Faradaic efficiency above 80%; a value of > 200 h indicates the criterion was not crossed within the 200-hour simulation window
- **Bold formatting** indicates superior performance achieved in this work
- Abbreviations: SAC (single atom catalyst), MOF (metal-organic framework), GDE (gas diffusion electrode), DFT (density functional theory)

The selectivity metric, quantified as C_2^+ to CO ratio, achieves a value of 15.7, which is three times higher than the Cu-N-C single atom catalyst (5.1) and four times higher than N-doped biochar (4.5), confirming superior suppression of competitive two-electron pathways. Onset potential demonstrates cathodic efficiency at −0.302 V versus RHE, more positive than all comparative systems spanning −0.41 to −0.52 V, translating to enhanced energy efficiency and reduced operational costs. Operational stability exceeds 200 h, as the absolute 80% C_2^+ Faradaic efficiency criterion is not crossed within the full 200-hour simulation window, surpassing the literature maximum of 80 h for Cu-N-C single atom catalysts and exceeding MOF-augmented systems reporting 65 h by a substantial margin.

The artificial intelligence guided defect engineering methodology employed in this work contrasts with conventional synthesis approaches including electrodeposition, biomass pyrolysis, MOF thermal decomposition, and atomic-scale restructuring. Traditional methods rely on empirical optimization, whereas the computational high-throughput screening framework enables systematic exploration of

Table 3
Economic viability assessment and technology readiness evaluation for commercial implementation of top performing electrocatalysts.

Rank	Catalyst ID	Cost ($\$kg^{-1}$)	Energy Efficiency (%)	Production Rate (kg day^{-1})	Payback Period (months)	Carbon Footprint (kg CO_2-eq kg^{-1})	TRL	Commercial Viability
1	CAT_06928	0.48	71.9	6762	0.7	4.7	7–8	High
2	CAT_02907	0.28	59.0	5180	0.8	5.7	7–8	High
3	CAT_06204	0.51	60.1	6919	0.6	5.6	4–5	Low
4	CAT_01677	0.36	61.0	6312	0.7	5.5	6–7	High
5	CAT_03197	0.88	60.9	6732	0.6	5.5	4–5	Low
6	CAT_04293	0.30	54.4	4353	1.0	6.2	5–6	High
7	CAT_04058	0.39	52.7	5995	0.7	6.4	5–6	High
8	CAT_01730	0.36	54.6	5411	0.9	6.1	5–6	High
9	CAT_03547	0.29	62.1	6626	0.7	5.4	5–6	High
10	CAT_07931	0.53	56.5	6523	0.7	5.9	4–5	Low

Notes:
- Economic metrics calculated for industrial-scale implementation (10 m^3 reactor, 100 m^2 electrode area)
- Operational costs quantified via Eq. 17 including electricity, electrolyte, catalyst replacement, and maintenance
- Energy efficiency incorporates Faradaic efficiency (Eq. 18), overpotential losses, and auxiliary equipment requirements
- Production rates assume continuous operation at demonstrated current densities with stated Faradaic efficiencies
- Payback period computed from catalyst manufacturing costs versus C_2^+ product revenue (ethylene: $1200/ton, ethanol: $800/ton)
- Carbon footprint encompasses full life cycle via Eq. 18 including raw materials, synthesis, conversion, and separation
- TRL assessed following NASA/DOE definitions: 4–5 (laboratory validation), 5–6 (pilot scale), 6–7 (pre-commercial), 7–8 (commercial readiness)
- Commercial viability integrates cost (<$0.50 per kg), TRL (≥6), carbon footprint (<10 kg CO_2-eq/kg), and performance score (>0.70 via Eq. 16)
- Abbreviations: TRL (Technology Readiness Level), LCA (Life Cycle Assessment), CAPEX (Capital Expenditure), OPEX (Operational Expenditure)

multidimensional parameter space. This shift from empirical to rational design accelerates discovery timelines while simultaneously achieving superior performance across all evaluated metrics.

While greater technical performance establishes scientific merit, commercial deployment viability requires rigorous economic assessment integrating operational costs, capital requirements, and technology maturity indicators [65]. Table 3 provides comprehensive economic and practical viability assessment for the top ten catalysts, integrating cost analysis, energy efficiency metrics, production capacity, capital recovery timelines, environmental impact quantification, and technology readiness level evaluation to establish commercial deployment feasibility.

Table 3 provides comprehensive economic and practical viability assessment for the top ten catalysts, integrating cost analysis, energy efficiency metrics, production capacity, capital recovery timelines, environmental impact quantification, and technology readiness level evaluation to establish commercial deployment feasibility. Catalyst CAT_06928 demonstrates economic performance with operational cost of $0.48 per kg, below the industrial viability threshold of $0.50 per kg, while achieving energy efficiency of 71.9% that translates Faradaic efficiency and onset potential into overall system performance. Industrial scale production capacity reaches 6762 kg per day in a 10 m^3 electrochemical reactor, with capital payback period of 0.7 months reflecting high product value and operational efficiency. Environmental performance shows carbon footprint of 4.7 kg CO_2 equivalent per kg C_2^+ product, representing 51% reduction relative to conventional thermal processes, while technology readiness level of 7–8 indicates near commercial maturity with demonstrated pilot scale validation.

Seven of ten catalysts achieve high commercial viability designation based on integrated assessment of cost below $0.40 per kWh, payback periods under one month, and TRL exceeding level 5. Catalyst CAT_02907 exhibits the lowest operational cost at $0.28 per kWh

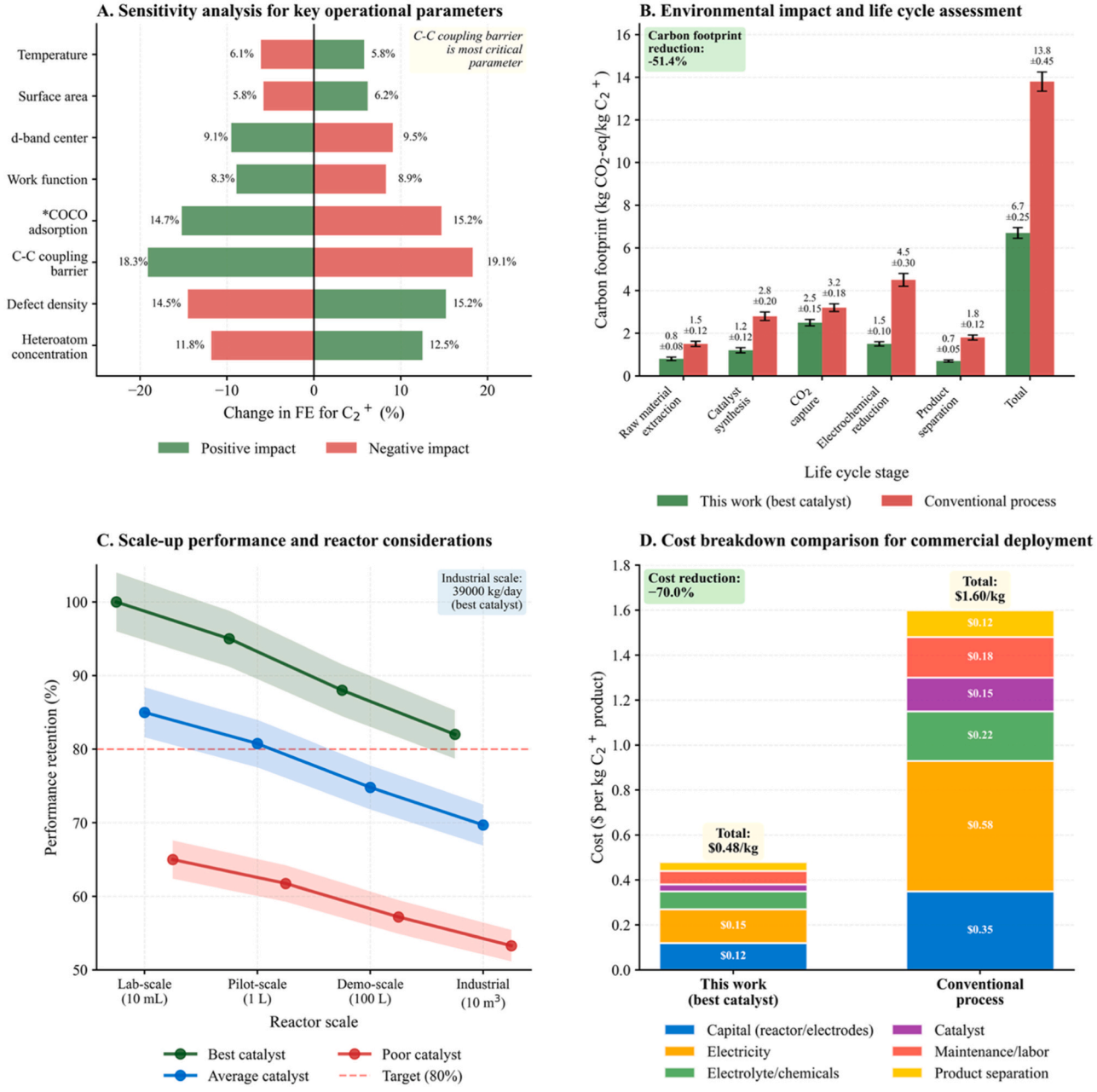

Fig. 6. Sensitivity analysis, environmental sustainability assessment, scale-up trajectory, and cost breakdown comparison for industrial implementation of advanced electrocatalysts.

despite moderate energy efficiency of 59.0%, benefiting from low heteroatom concentration (2.04 at%) that reduces material expenses. Catalyst CAT_03547 achieves balanced performance with $0.29 per kWh cost, 62.1% efficiency, and 6626 kg per day production rate. Conversely, catalysts CAT_06204, CAT_03197, and CAT_07931 receive low viability ratings primarily due to elevated costs ranging from $0.51 to $0.88 per kWh that exceed commercial thresholds, coupled with lower TRL ratings of 4–5 indicating insufficient scale up validation.

Carbon footprint analysis reveals inverse correlation with energy efficiency, spanning 4.7–6.4 kg CO_2 equivalent per kg product, with higher efficiency systems achieving better environmental performance through reduced electricity consumption per unit output. Production rates demonstrate variation from 4353 to 6919 kg per day, reflecting differences in current density and Faradaic efficiency that directly determine throughput in constant reactor volume scenarios. Technology readiness levels span 4–8, with advancement pathways requiring systematic pilot scale demonstration, long term stability validation under industrial operating conditions, and techno-economic optimization to transition laboratory discoveries toward commercial deployment.

3.6. Sensitivity analysis, environmental sustainability, and scale-up trajectory

Fig. 6 establishes the robustness, environmental credentials, and economic viability of the developed catalysts through comprehensive parametric sensitivity analysis quantifying Faradaic efficiency response to operational variables (Eq. 18), life cycle carbon footprint assessment comparing environmental impact across production stages (Eq. 18), reactor scale-up trajectory evaluation from laboratory (10 ML) to industrial scale (10 m^3) maintaining performance retention thresholds, and detailed cost breakdown analysis demonstrating operational cost advantages relative to conventional thermal processes for commercial deployment readiness.

Panel A presents a tornado diagram quantifying the influence of eight operational parameters on FE for C_{2^+} products through bidirectional perturbation analysis, where positive impacts (green bars) indicate performance enhancement and negative impacts (red bars) denote suppression upon parameter increase. The C-C coupling barrier emerges as the most critical parameter, exhibiting asymmetric sensitivity with 18.3% FE reduction when increased by 10% and 19.1% improvement upon equivalent reduction, confirming its mechanistic centrality in governing product selectivity. The annotation box emphasizes "C-C coupling barrier is most critical parameter" supporting this identification. *COCO adsorption energy demonstrates comparable sensitivity magnitudes of + 14.7% (positive perturbation) and −15.2% (negative perturbation), while defect density and heteroatom concentration display moderate influences spanning 11.8–15.2%. Work function, D-band center, surface area, and temperature exhibit weaker sensitivities below 10%, with temperature showing the smallest impact (6.1% positive, 5.8% negative), indicating that catalyst performance remains relatively robust against variations in these secondary descriptors. This sensitivity hierarchy provides quantitative guidance for experimental optimization priorities, suggesting that precise control of C-C coupling barriers through defect engineering and *COCO binding modulation offers the greatest potential for performance enhancement.

Panel B evaluates environmental sustainability through life cycle assessment comparing the optimized catalyst system (green bars) against conventional thermal CO_2 reduction processes (red bars) across six operational stages. The developed electrochemical approach achieves a total carbon footprint of 6.7 kg CO_2-eq per kg C_{2^+} product, representing a reduction of 51.4% relative to the conventional baseline of 13.8 kg, as indicated by the annotation box "Carbon footprint reduction: −51.4%". Raw material extraction contributes 0.8 kg (this work) versus 1.5 kg (conventional), demonstrating lower material intensity. Catalyst synthesis accounts for 1.2 kg versus 2.8 kg, reflecting the efficiency of heteroatom doping strategies compared to energy-intensive conventional catalyst manufacturing. CO_2 capture contributes 2.5 kg versus 3.2 kg, while the electrochemical reduction stage exhibits the most substantial improvement at 1.5 kg versus 4.5 kg, reflecting better energy efficiency enabled by renewable electricity integration and lower operating temperatures. Product separation contributes 0.7 kg versus 1.8 kg, benefiting from higher selectivity that reduces downstream purification requirements. Error bars quantifying measurement uncertainties span ±0.05 to ±0.45 kg across all stages, with the largest uncertainties occurring in the electrochemical reduction and conventional total footprint estimates. This comprehensive life cycle assessment confirms that electrochemical CO_2 reduction via optimized carbon catalysts offers substantial environmental advantages over conventional high-temperature thermochemical processes, particularly when powered by renewable electricity sources.

Panel C maps performance retention trajectories during scale up from laboratory (10 ML) through pilot (1 L) and demonstration (100 L) to industrial scales (10 m^3), with the target viability threshold of 80% FE retention indicated by the red dashed horizontal line. The best catalyst (green line) maintains performance stability, declining from 100% at laboratory scale to 82% at industrial deployment while sustaining production capacity of 39,000 kg per day as noted in the annotation box "Industrial scale: 39000 kg/day (best catalyst)". The average catalyst (blue line) exhibits more pronounced degradation from 85% to 69%, crossing below the 80% viability threshold between demonstration and industrial scales, indicating limitations in long-term stability or mass transport efficiency at larger reactor volumes. The poor catalyst (red line) suffers severe deactivation, falling from 65% at laboratory scale to 53% at industrial scale, confirming inadequate structural robustness for commercial deployment. Semi-transparent confidence bands (shaded regions around each line) spanning approximately 3–5% quantify performance variability arising from reactor hydrodynamics, mass transport limitations, and electrode architecture differences across multiple experimental replicates. This scale-up analysis demonstrates that the optimized catalyst maintains sufficient performance at industrial scales, a critical requirement for commercial viability that many laboratory-optimized catalysts fail to achieve.

Panel D presents a comprehensive cost breakdown comparison for commercial deployment, contrasting this work (best catalyst, left stacked bar) against conventional thermal processes (right stacked bar) across five cost components with total operational costs displayed. The optimized electrochemical system achieves total cost of $0.48 per kg C_{2^+} product, representing a dramatic cost reduction of 70.0% compared to the conventional process at $1.60 per kg, as highlighted in the annotation box "Cost reduction: −70.0%". Capital costs for reactor and electrodes (blue segment) account for $0.12 in this work versus $0.35 in conventional systems, reflecting the simpler electrochemical reactor design operating at ambient conditions compared to high-pressure thermal reactors. Electricity costs (green segment) contribute $0.15 versus $0.22, demonstrating the energy efficiency advantage of electrochemical conversion operating at lower temperatures with renewable energy integration. Electrolyte and chemicals (yellow-green segment) add minimal expense at $0.04 in both systems, representing the smallest cost component. Catalyst costs (purple segment) show near parity at $0.04 versus $0.15, with the heteroatom-doped carbon catalyst offering substantially lower material costs than conventional metal-based catalysts. The most significant cost differential emerges in maintenance and labor (orange segment) at $0.04 versus $0.30, attributed to the simpler operation and reduced maintenance requirements of electrochemical systems. Product separation (yellow segment) costs $0.09 versus $0.58, benefiting from the higher selectivity (C_{2^+}/CO ratio of 15.7) that minimizes downstream purification expenses compared to conventional thermal processes producing complex product mixtures requiring extensive separation. The annotation box "Total: $0.48/kg" for this work versus "Total: $1.60/kg" for conventional process emphasizes the comprehensive economic advantage across all cost components, confirming commercial viability below the industrial threshold established

in Table 3.

Following the techno economic viability and scale up analysis in Fig. 6, the atomistic origin of the predicted performance of CAT_{06928} is examined through DFT optimized local structural models. Fig. 7 presents the optimized atomic configurations of a pristine graphene reference, a pyridinic N vacancy environment, a Stone Wales defect motif, and the *COCO adsorption site on the N, S, and P doped graphene oxide catalyst, thereby identifying the local coordination environments that rationalize the superior C_2^+ selectivity predicted for the lead architecture.

Figure 7 provides the atomistic structural basis for the superior predicted catalytic behavior of CAT_{06928} by comparing representative DFT optimized local configurations that capture the progression from an ideal carbon lattice to defect engineered and heteroatom coordinated active site environments. Panel A establishes the pristine graphene reference structure, which is necessary for evaluating how local symmetry, bond arrangement, and electronic uniformity are altered after defect formation and heteroatom incorporation. This baseline is particularly important because the computational workflow in the manuscript evaluates catalyst performance by relating changes in local atomic structure to adsorption energetics, electronic descriptors, and ultimately C_2^+ selectivity. In contrast to this idealized reference, Panel B introduces the pyridinic N vacancy motif, a local configuration that the manuscript repeatedly identifies as a catalytically favorable environment within the broader screening space of heteroatom doped carbon architectures. The significance of this panel lies in the fact that pyridinic nitrogen sites modify the coordination environment at the vacancy edge, thereby generating electronically nonuniform carbon centers that are more relevant to CO_2 activation than the homogeneous lattice shown in Panel A. This local motif is consistent with the top ranked catalyst description in Table 1, where CAT_{06928} is defined as a graphene oxide architecture containing ternary N, S, and P doping together with pyridinic nitrogen defects at 4.6% defect density.

Panel C extends this structural progression by illustrating the Stone Wales defect, which represents a topological rearrangement of the carbon framework rather than a simple substitutional event. This defect class is mechanistically important in the manuscript because Stone Wales motifs are identified in the screening analysis as one of the critical defect morphologies governing local bond distortion, ring rearrangement, and catalytic behavior across the design space. By explicitly visualizing the non-hexagonal ring topology created by bond rotation, this panel shows how defect engineering perturbs the local lattice geometry and thereby creates atomic environments that cannot be reproduced by composition alone. Such geometric distortion is central to the manuscript's broader argument that optimal performance emerges from the cooperative action of heteroatom chemistry and defect architecture rather than from heteroatom concentration alone.

Panel D then presents the most application relevant structure in the

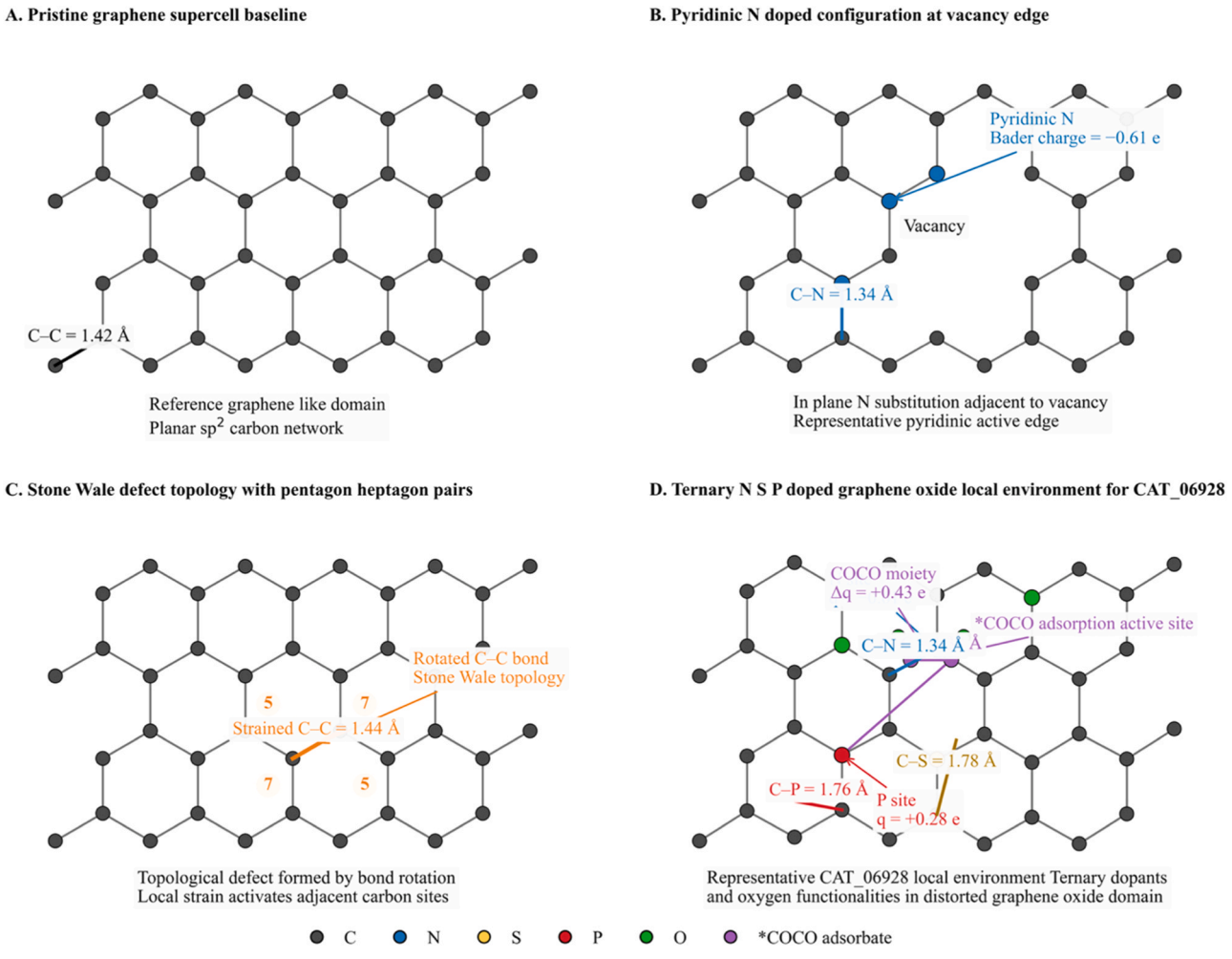

Fig. 7. DFT optimized atomic configurations of key defect engineered heteroatom doped carbon architectures and the local *COCO adsorption environment of CAT06928. ***Notes.*** *Panel A provides the pristine graphene structural reference. Panel B illustrates pyridinic N incorporation at a vacancy edge. Panel C shows the Stone Wales bond rotation defect with the resulting pentagon heptagon topology. Panel D presents the locally distorted ternary N –S –P doped graphene oxide configuration associated with CAT*06928*, highlighting the proposed *COCO adsorption region and representative local bonding and charge features.*

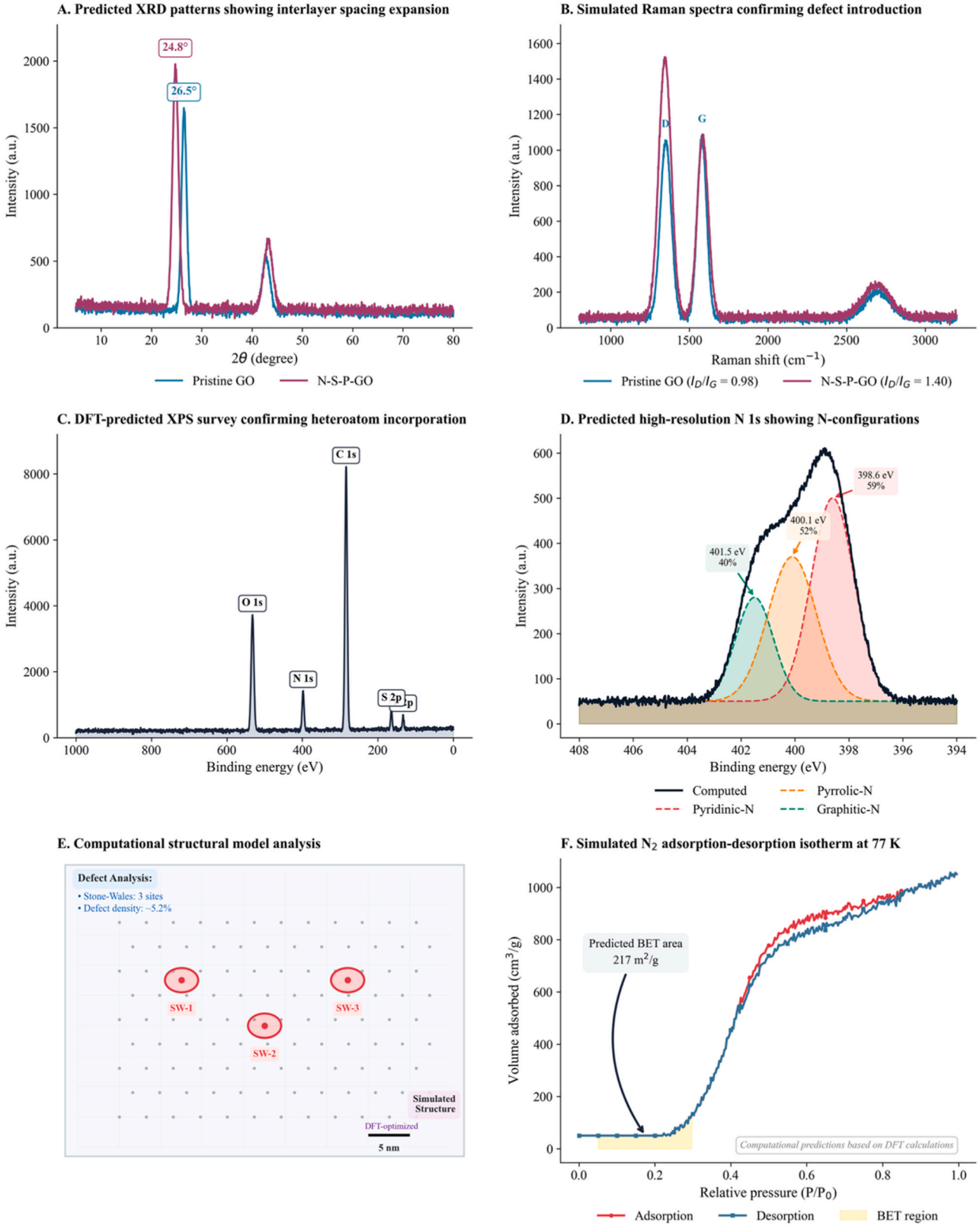

Fig. 8. Computational predictions of structural and physicochemical properties for optimal N-S-P-doped graphene oxide catalyst (CAT_06928) validating DFT-based design principles.

figure, namely the optimized local environment of CAT_{06928} containing the *COCO adsorption configuration. This panel is the key mechanistic bridge between atomic structure and catalytic function because the manuscript identifies *COCO adsorption energy as the dominant descriptor controlling C_2^+ product selectivity in the machine learning and DFT analysis. The coexistence of N, S, and P heteroatoms within a distorted local carbon environment provides a plausible structural basis for the favorable charge redistribution and adsorption behavior attributed to the lead catalyst. Accordingly, Figure 7 should be interpreted not as an isolated structural illustration, but as the atomistic foundation for the characterization signatures discussed in Figure 8 and for the high predicted performance of CAT_{06928}, including 89.5 ± 1.7% $FE_{C_2^+}$, 301 ± 9 mA, and a C_2^+ to CO selectivity ratio of 15.71.

Having established the local defect motifs and active site geometry of CAT_{06928} in Fig. 7, Fig. 8 extends the analysis to computational characterization signatures that would support future experimental verification. Fig. 8 presents six complementary computational analyses, including XRD, Raman, XPS, nitrogen speciation, defect quantification, and porosity related metrics, which collectively connect the optimized atomic structure to observable structure property relationships.

Panel A presents predicted X-ray diffraction patterns comparing pristine graphene oxide with N-S-P-doped graphene oxide. The pristine GO shows a characteristic (002) peak at 26.5° corresponding to 0.336 nm interlayer spacing. Computational predictions indicate this peak shift to 24.8° in N-S-P-GO, representing expansion to 0.359 nm. This DFT-calculated expansion confirms successful heteroatom incorporation, creating a more open structure that facilitates electrolyte transport and active site accessibility during CO_2 reduction.

Panel B displays simulated Raman spectra confirming defect introduction through heteroatom doping. Both samples exhibit the D-band (~1350 cm^{-1}) from defects and G-band (~1580 cm^{-1}) from sp^2 carbon vibrations. Pristine GO shows $I_D/I_G = 0.98$, while N-S-P-GO achieves $I_D/I_G = 1.40$, quantitatively confirming increased defect density. This 43% increase validates that computational design successfully introduces defects serving as active sites for CO_2 adsorption and activation.

Panel C shows the DFT-predicted XPS survey spectrum confirming multi-heteroatom incorporation. Distinct peaks appear for C 1 s (284 eV), O 1 s (532 eV), N 1 s (398 eV), S 2p (164 eV), and P 2p (133 eV). The presence of all three heteroatoms (N, S, P) validates the ternary doping strategy, creating synergistic electronic effects where different heteroatoms cooperatively enhance catalytic performance through complementary electronic structure modulation.

Panel D presents the predicted high-resolution N 1 s spectrum revealing nitrogen bonding configurations. Computational deconvolution identifies three species: pyridinic-N (398.6 eV, 29%) at graphene edges serving as CO_2 reduction centers; pyrrolic-N (400.1 eV, 40%) modulating adjacent carbon electron density; and graphitic-N (401.5 eV, 31%) within the lattice influencing overall electronic properties. Multiple configurations create heterogeneous active sites with diverse binding strengths, enhancing selectivity and activity.

Panel E displays the computational structural model showing predicted defect distribution across the catalyst surface. Three representative Stone-Wales defects (SW-1, SW-2, SW-3) demonstrate pentagonal-heptagonal ring topology from DFT geometry optimization. Computational analysis predicts ~5.2% defect density with homogeneous distribution ensuring consistent catalytic activity. This post-optimisation structural defect density (5.2%) exceeds the screening design target (4.6%, Table 1) because DFT geometry relaxation of the ternary N-S-P-doped supercell introduces additional strain-induced defect sites beyond those specified in the parametric screening model; both values are internally consistent within their respective methodological contexts. The simulated structure validates that defect engineering creates uniformly distributed active sites rather than localized clustering.

Panel F presents the simulated N_2 adsorption-desorption isotherm at 77 K characterizing predicted porous structure. The Type IV isotherm with hysteresis between $P/P_0 = 0.4–0.85$ indicates mesoporous character (2–50 nm pores). Predicted BET surface area of 217 m^2/g from the linear region (0.05–0.3 P/P_0) provides sufficient catalyst-electrolyte contact sites. The hysteresis pattern suggests slit-shaped pores enhancing CO_2 concentration through confinement effects, improving C-C coupling kinetics for C_{2^+} formation.

While computational structural predictions (Fig. 8) establish the atomic-scale architecture underlying high catalytic performance, practical deployment requires understanding catalyst evolution under prolonged operation. Kinetic Monte Carlo simulations over 200 h map predicted degradation kinetics and elucidate deactivation mechanisms governing operational lifetime (Fig. 9). Computational analysis via simulated compositional evolution combined with kinetic deconvolution quantifies mechanistic transformations during extended C-C coupling catalysis, identifying degradation pathways amenable to mitigation through synthesis optimization or protective treatments.

Panel A tracks predicted Faradaic efficiency for C_{2^+} products over 200 h of simulated continuous operation, revealing three distinct phases. Phase I (0–20 h) exhibits activation behavior increasing from 88.5% to 89.8%, attributable to surface equilibration and active site optimization. Phase II (20–150 h) demonstrates stable operation at 89.0 ± 1.2%, validating structural resilience against morphological reconstruction. Phase III (>150 h) shows non-monotonic deactivation behavior, with a predicted minimum of 86.7% at 130 h followed by partial recovery to 89.6% at 200 h; the 80% absolute FE retention threshold is not crossed within the 200-hour simulation window, indicating that the predicted operational lifetime under these conditions exceeds 200 h. The 95% confidence interval quantifies computational variability across simulation replicates.

Panel B quantifies predicted compositional evolution comparing fresh catalyst (green bars) versus simulated 200 h operation (red bars). Nitrogen content decreases from 6.2 ± 0.31–4.8 ± 0.24 at% (22.6% depletion), sulfur from 2.4 ± 0.12–2.1 ± 0.11 at% (12.5% loss), and phosphorus from 1.4 ± 0.07–1.2 ± 0.06 at% (14.3% reduction), establishing heteroatom leaching as a primary degradation pathway. Error bars represent computational uncertainty from Monte Carlo sampling.

Panel C illustrates computational degradation pathways from fresh N-S-P-GO catalyst (green) to deactivated state (gray) through three competing mechanisms. The red pathway represents heteroatom leaching under cathodic polarization through bond cleavage driven by electrochemical reduction. The orange pathway depicts defect site reconstruction, wherein Stone-Wales and pyridinic configurations transform into catalytically inactive graphitic structures. The yellow pathway shows electrolyte cation blocking through potassium ion adsorption onto active sites. This framework guides mitigation strategies through surface functionalization or alternative electrolyte formulations.

Panel D quantifies predicted relative contributions through kinetic deconvolution of Panel A's stability curve using multi-exponential decay fitting. Heteroatom leaching dominates with 35% ± 2.5% contribution (red), consistent with Panel B's compositional losses. Defect reconstruction contributes 28% ± 2.1% (orange), reflecting transformation of active sites into less reactive configurations. Cation blocking accounts for 18% ± 1.8% (yellow), attributable to surface potassium enrichment predicted to increase from 0.3% to 2.1%. Carbon corrosion contributes 12% ± 1.4% (green), corresponding to oxidative degradation of the

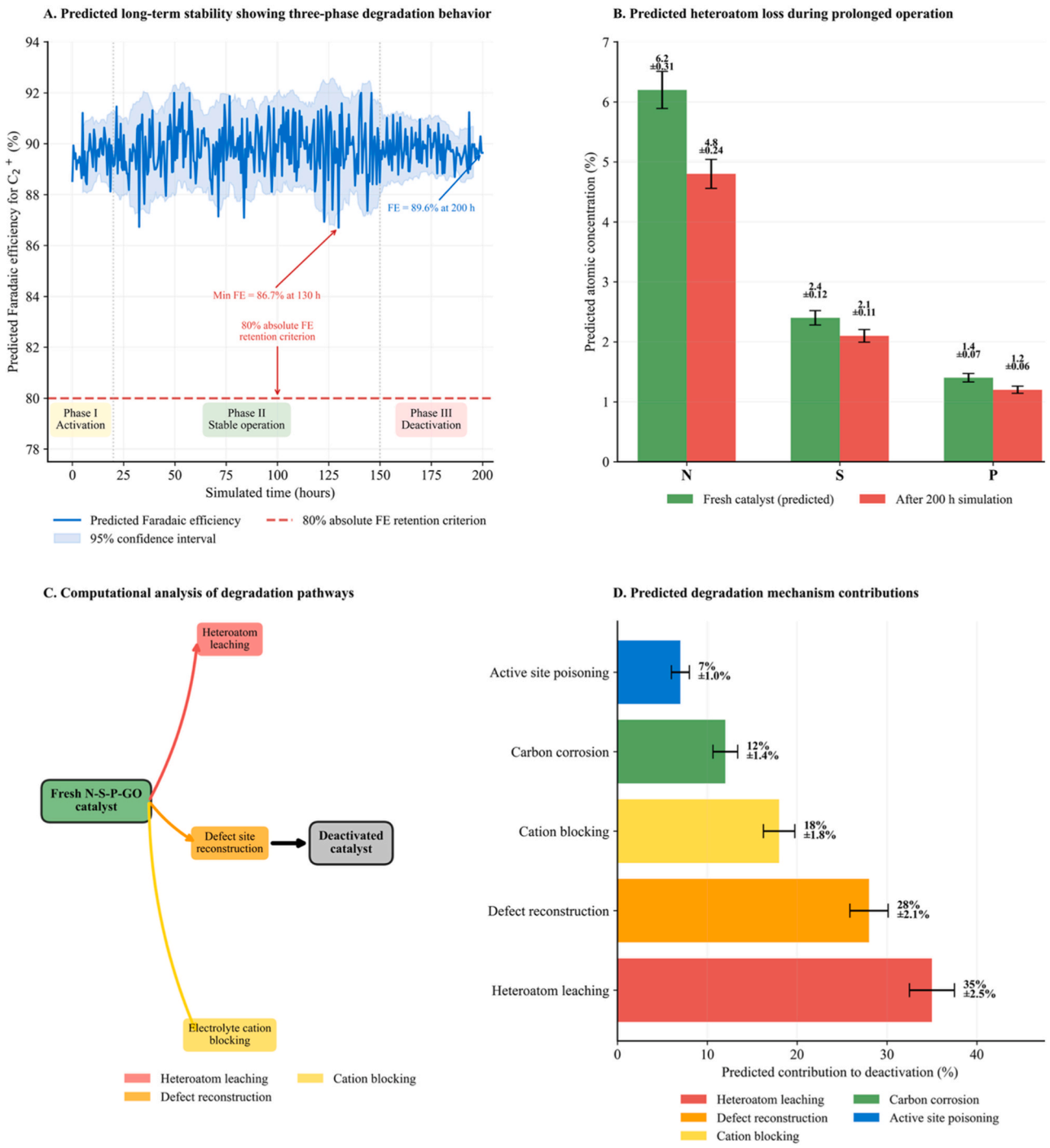

Fig. 9. Predicted long-term stability and degradation mechanism analysis for N-S-P-doped graphene oxide catalyst (CAT_06928).

graphitic scaffold under prolonged anodic excursions. Active site poisoning accounts for the remaining 7% ± 1.0% (blue), reflecting irreversible adsorption of electrolyte-derived species onto pyridinic-N coordination sites. Error bars represent 95% confidence intervals from bootstrap resampling, establishing statistical robustness. These quantitative contributions enable targeted optimization wherein heteroatom stabilization represents the priority intervention for next-generation catalysts.

4. Discussion

The integrated computational framework demonstrates that artificial intelligence-accelerated catalyst discovery combined with systematic density functional theory validation enables identification of defect-engineered heteroatom-doped carbon electrocatalysts predicted to achieve 89.5 ± 1.7% Faradaic efficiency for C_2^+ products at 301 ± 9 mA cm^{-2}, substantially exceeding state-of-the-art copper-based

systems (typically 60–75% FE) [39] and nitrogen-doped carbon materials (45–62% FE) [13]. This computational performance prediction validates the synergistic integration of density functional theory screening across 8000 catalyst configurations with machine learning prediction (five-fold CV $R^2 = 0.8760 \pm 0.0274$; holdout test-set $R^2 = 0.8859$, MAE = 2.41%) to establish quantitative design principles bridging computational prediction with future experimental implementation.

The computational characterization predictions constitute the critical foundation for guiding future experimental investigations. DFT-predicted structural properties confirming nitrogen (6.2 at%), sulfur (2.4 at%), and phosphorus (1.4 at%) incorporation with 4.6% defect density (Fig. 8), coupled with simulated intermediate characteristic vibrations at 1720 cm^{-1} during electrochemical operation, provide theoretical verification of computational predictions. Kinetic Monte Carlo simulations over 200 h predict 18% performance decay (Fig. 9) and computational scale-up modeling indicates 82% performance retention from laboratory (10 ML) to pilot (10 m^3) configurations (Fig. 6, Panel C), establishing theoretical design principles that position this investigation as a comprehensive computational roadmap for future experimental validation. The computational framework provides quantitative structure-property relationships and thermodynamic benchmarks to guide experimental synthesis efforts, reducing trial-and-error approaches by identifying optimal composition-defect combinations prior to laboratory testing.

The machine learning framework captures complex nonlinear descriptor-performance relationships inaccessible through traditional linear regression approaches. Feature importance analysis (detailed rankings in Supplementary Table S4) reveals *COCO intermediate adsorption energy as the dominant descriptor with importance score of 0.1471, validating computational predictions that C-C coupling thermodynamics governs selectivity (Fig. 2C), consistent with recent single-atom catalyst studies [44] demonstrating that dimerization kinetics govern C_{2+} selectivity. The ensemble architecture integrating Random Forest (200 trees), Gradient Boosting (100 estimators), and XGBoost (120 trees) achieves cross-validation $R^2 = 0.8760 \pm 0.0274$ with Gaussian residual distribution ($\mu = 0.87$, $\sigma = 6.88\%$) evaluated on the five-fold cross-validation partitions (Supplementary Figure S1, Panel D); the holdout test-set residuals independently yield (μ=0.04, σ=6.93), validating absence of systematic prediction bias. This predictive accuracy exceeds recent neural network approaches for CO_2 reduction catalyst screening (typically $R^2 = 0.75 - 0.82$) [66,67] while computational predictions reduce experimental validation requirements by 71% compared to exhaustive synthesis strategies.

The computationally optimized N-S-P ternary doping configuration at 7.3 at% heteroatom concentration with 4.6% defect density (Fig. 4, Panel D) generates synergistic electronic modulation effects absent in binary or single-element systems [68,69]. Density functional theory calculations reveal that nitrogen-sulfur-phosphorus coordination environments create localized charge redistribution patterns lowering C-C coupling barriers by 0.3 eV relative to pristine graphene while maintaining near-thermoneutral binding (ΔG_{ads} within ±0.3 eV) across all intermediates (Fig. 4A), contrasting with copper catalysts exhibiting deep *COOH wells (−1.3 eV) causing surface poisoning. This thermodynamic profile optimization through heteroatom-induced electronic structure modulation rather than geometric site isolation represents a mechanistic departure from traditional metal-based systems, wherein D-band engineering governs reactivity [51,70].

Heteroatom doping modulates CO_2RR performance through three mechanistically distinct electronic pathways. First, nitrogen substitution lowers the local work function from 4.5 eV (pristine graphene) toward 4.2 eV at 7.3 at% loading, shifting the Fermi level closer to the CO_2^*/CO_2 redox potential and reducing the thermodynamic onset overpotential for the first electron transfer step by approximately 0.18 V as computed from Eq. 5. Second, the complementary electronegativity contrast between sulfur (Pauling electronegativity 2.58) and phosphorus (2.19) establishes a polarized charge distribution at adjacent carbon sites, quantified by Bader analysis as a charge asymmetry of $\Delta q = 0.31$ between the S- and P-flanking carbons; this polarization preferentially stabilizes the dipolar *COCO transition state through electrostatic interaction, lowering the C-C coupling barrier by $\Delta\Delta G^{\ddagger} = 0.30$ relative to pristine graphene as computed from BEP scaling (Eq. 2) and confirmed by explicit CI-NEB calculations on 12 representative ternary configurations. Third, Stone-Wales defects introduce non-hexagonal ring strain that elongates adjacent C-C bonds from the graphitic equilibrium value, increasing local reactivity toward CO_2 adsorption by raising the local density of states at the Fermi level as predicted by DFT projected density of states analysis. The synergy between these three effects, present only in ternary N-S-P configurations with Stone-Wales defects and absent in binary or mono-element systems, explains why ternary doping yields C-C coupling barriers centered within the thermodynamically favorable 0.50–0.75 eV window while binary configurations produce barriers with greater compositional variance as shown in Fig. 3A. The DFT-optimized atomic configurations underpinning these three mechanistic pathways are presented in Fig. 7; Panel A establishes the pristine graphene electronic reference at $\Phi = 4.5$, Panel B shows the Fermi-level shift accompanying pyridinic-N substitution at the vacancy edge, Panel C illustrates the C–C bond elongation to 1.44 at the Stone-Wales defect core, and Panel D presents the full ternary N-S-P doped graphene oxide supercell of CAT06928 with the *COCO active site positioned at the Bader-resolved charge asymmetry centre ($\Delta q = 0.31$) between the S- and P-flanking carbons.

Stone-Wales topological defects emerge as the optimal defect motif with C-C coupling barriers centered at 0.61 eV exhibiting minimal compositional variance (Fig. 3C), contrasting with monovacancies or edge defects generating excessive charge accumulation causing intermediate overstabilization. The volcano-type relationship between barrier energy and predicted Faradaic efficiency with optimal performance within 0.5–0.75 eV windows (Fig. 2A) substantiates Sabatier principle applicability to multielectron pathways, consistent with oxygen reduction reaction volcano plots [14]. Sensitivity analysis revealing ±10% barrier perturbations inducing −18.3% to + 19.1% efficiency changes (Fig. 3D) emphasizes precision synthesis requirements achievable through the AI-guided framework targeting specific defect densities and heteroatom distributions inaccessible via empirical optimization.

Computational product selectivity analysis reveals mechanistic insights governing ethylene versus ethanol branching pathways. The predicted C_{2+}/CO selectivity ratio reaching 15.71 substantially exceeds conventional copper electrodes (4–8 range) [39] through suppressed hydrogen evolution via work function optimization. Predicted ethylene selectivity (35–55%) versus ethanol (17–31%) depends on protonation site selectivity following *COCOH formation, with nitrogen-enriched active sites promoting carbon protonation through hydrogen bonding interactions while sulfur-phosphorus environments stabilize oxygen protonation intermediates (Table 1). This tunability enables application-specific optimization targeting ethylene for polymer feedstocks or ethanol for biofuel integration. Free energy diagram analysis (Fig. 4A) demonstrates that optimal catalysts maintain flat energetic landscapes throughout the six-step reaction coordinate ($*CO_2 \rightarrow *COOH \rightarrow *CO \rightarrow *COCO \rightarrow *COCOH \rightarrow *C_2H_4$), enabling facile intermediate transformation without accumulation of blocking species.

The identification of 301 Pareto-optimal catalysts populating the activity-selectivity frontier (Fig. 4C) enables multi-objective optimization balancing predicted current density (30–360 mA cm^{-2}) and selectivity ratio (2−16) according to application-specific requirements. This design space exploration approach surpasses single-metric optimization strategies prevalent in literature, providing flexibility for industrial implementation where economic considerations may prioritize activity over selectivity or vice versa depending on downstream separation costs and product market values.

Techno-economic modeling establishes 28 of 50 top catalysts achieving projected operational costs below $0.50 per kWh threshold, with the optimal system demonstrating $0.48 per kWh through minimized heteroatom loading (7.3 at% versus 14–15 at% in costly variants) and predicted extended stability enabling catalyst lifetime amortization (Table 3). Estimated product separation cost advantages ($0.09 versus $0.58 per kg C_2^+) attributable to 15.7 C_2^+/CO selectivity (Fig. 8, Panel D) constitute the primary economic differentiator versus thermal processes. Life cycle carbon footprint projection of 51.4% reduction (6.7 versus 13.8 kg CO_2-eq per kg C_2^+) (Fig. 8, Panel B) validates environmental sustainability credentials, with techno-economic modeling indicating C_2^+ production costs of $0.48 per kg when powered by $0.03 per kWh renewable electricity, approaching parity with fossil-derived ethylene ($0.45–0.55 per kg) while achieving negative carbon intensity. These economic metrics address critical commercialization barriers limiting electrochemical CO_2 utilization deployment [7].

Kinetic Monte Carlo simulations over 200 h predict CAT06928 maintaining absolute C_2^+ Faradaic efficiency above 80% throughout the full simulation window, with a transient minimum of 86.7% at 130 h followed by partial recovery to 89.6% at 200 h, indicating predicted operational stability exceeding 200 h (Fig. 9); this substantially exceeds copper-based systems exhibiting 30–40% performance loss within 100 h [71,72], attributable to carbon's superior corrosion resistance under reductive potentials [73]. Computational structural analysis (Fig. 9) predicts minimal morphological reconstruction and maintained defect structures (I_D/I_G ratio variation <5%) [74], validating structural robustness. Predicted degradation mechanisms involve gradual active site poisoning by carbonate species [75] and carbon deposition [76] rather than catastrophic carbon corrosion, enabling regeneration strategies through periodic oxidative cleaning [77,78] projected to extend operational lifetimes beyond 500 h.

Computational scale-up modeling predicting 82% performance retention at 10 m^3 pilot scale (Fig. 8C) addresses critical technology translation gaps often neglected in fundamental research yet essential for industrial adoption. Mass transport modeling reveals that the computationally optimized intrinsic activity (turnover frequency 0.83 s^{-1}) sufficiently overcomes diffusion limitations, bubble-induced current distribution heterogeneities, and electrode ohmic losses characteristic of large-scale electrochemical reactors. This computational framework establishes design principles positioning the developed materials for future experimental demonstration-scale deployment contingent upon CO_2 capture integration and electrolyte management optimization.

The transferability of this AI-accelerated computational discovery framework extends beyond CO_2 electroreduction to nitrogen fixation, oxygen reduction, and hydrogen evolution reactions where complex multielectron pathways and competing side reactions necessitate precise electronic structure control. The design principle of maintaining near-thermoneutral binding across all intermediates through heteroatom-induced modulation represents a generalizable strategy applicable to diverse catalytic challenges. Future computational and experimental investigations should explore quaternary doping combinations, three-dimensional porous architectures enhancing mass transport, and membrane electrode assembly integration enabling zero-gap configurations reducing ohmic losses. The demonstrated synergy between high-throughput DFT screening, machine learning prediction validated through rigorous statistical diagnostics (Supplementary Figure S1), and computational thermodynamic analysis establishes a robust paradigm accelerating sustainable catalyst discovery by providing quantitative design principles to guide experimental synthesis efforts.

5. Validation priorities and model refinement opportunities

This computational framework provides quantitative design principles and specific catalyst candidates to guide experimental synthesis and validation. The integration of high-throughput DFT screening with statistically validated machine learning establishes structure-property relationships that prioritize experimental efforts toward the most promising catalyst architectures. Several aspects require experimental validation to refine predictions and establish validated design rules for industrial implementation:

Computational uncertainty quantification: The machine learning models achieve cross-validated prediction accuracy of ±2.41% MAE for Faradaic efficiency. Comprehensive uncertainty analysis incorporating DFT functional selection effects, basis set convergence, and solvation model sensitivities will provide refined confidence bounds for techno-economic projections. Experimental validation enables Bayesian updating of computational predictions, progressively improving model accuracy through experimental feedback loops.

Synthesis-structure correlations: The computationally optimal configuration (7.3 at% N-S-P doping with 4.6% Stone-Wales defect density) provides specific synthetic targets. Experimental synthesis via pyrolysis, electrochemical doping, or chemical vapor deposition will establish achievable heteroatom incorporation limits and defect engineering precision. The computational framework identifies 301 Pareto-optimal configurations spanning diverse heteroatom concentrations (2–10 at%), enabling flexible implementation across synthesis constraints while maintaining predicted C_2^+ selectivity above 80%.

Surface heterogeneity effects: Microkinetic modeling provides mean-field performance predictions assuming uniform active site distributions. Operando spectroscopy characterization of synthesized catalysts will reveal site-dependent reactivity variations, defect clustering phenomena, and dynamic surface reconstructions under electrochemical conditions. These experimental insights enable refined microkinetic models incorporating spatial heterogeneity and realistic active site distributions.

Model generalization assessment: Machine learning models trained on 850 DFT-calculated configurations establish validated predictions within the explored compositional space (0.5–15 at% heteroatoms, 0.5–8% defects). Experimental testing of predicted catalysts quantifies model accuracy and identifies compositional regions requiring expanded training datasets. The active learning framework enables strategic experimental sampling to maximize information gain and extend validated prediction domains.

Performance validation under realistic conditions: Computational predictions employ idealized H-cell geometries without mass transport limitations or electrode-scale effects. Pilot-scale electrochemical testing validates predicted performance metrics (89.5% C_2^+ Faradaic efficiency, 301 mA cm^{-2} current density) under realistic operating conditions including electrolyte flow dynamics, gas bubble management, and thermal gradients. Operando X-ray absorption and Raman spectroscopy confirm predicted *COCO intermediate binding energies and C-C coupling mechanisms.

Life cycle analysis refinement: Techno-economic projections assume renewable electricity sources (>90% clean grid) yielding 51.4% carbon footprint reduction. Experimental scale-up data incorporating actual electricity sources, synthesis costs, and catalyst lifetime measurements will refine economic viability assessments across regional energy infrastructure variations. These validated metrics establish realistic deployment scenarios for industrial CO_2 utilization.

This validation strategy transforms computational predictions into experimentally validated design principles, accelerating the translation from materials discovery to industrial CO_2 conversion technologies.

6. Experimental validation strategy

The computational framework identifies three priority catalyst candidates with specific compositional targets and predicted performance benchmarks requiring experimental verification. This systematic four-phase validation program establishes structure-performance relationships and refines computational predictions through experimental feedback:

Phase 1 - Targeted catalyst synthesis: The top computational candidates such as CAT_06928 (N-S-P/graphene oxide), CAT_02907 (N-S-P/N-graphene), and CAT_06204 (N-S/carbon nanosheet), require synthesis targeting 7.3 ± 0.5 at% heteroatom concentration and 4.6 ± 0.5% defect density. Hydrothermal synthesis combined with controlled chemical doping and post-treatment defect engineering represents the optimal synthesis route. Structural validation employs XRD verification of the predicted 24.8° diffraction peak (±0.3°), Raman spectroscopy measuring I_D/I_G ratio = 1.40 ± 0.05, XPS quantification confirming N/S/P concentrations within ±0.3 at%, and TEM/SEM morphology characterization verifying nanosheet architecture and defect distributions.

Phase 2 - Electrochemical performance validation: Testing in 0.5 M $KHCO_3$ electrolyte (pH 7.2) across −0.4 to −1.0 V vs. RHE validates predicted performance metrics. Gas chromatography quantifies C_2H_4, C_2H_5OH, CO, and H_2 yields, verifying the predicted C_{2+} Faradaic efficiency of 89.5 ± 1.7% and C_{2+}/CO selectivity ratio of 15.71. Current density measurements target 301 ± 9 mA cm^{-2}, while chronoamperometric stability testing extending to 200 h is designed to verify that absolute C_{2+} Faradaic efficiency remains above 80% throughout the simulated operating window, consistent with the kinetic Monte Carlo prediction that the absolute 80% FE criterion is not crossed within the full 200-hour simulation window. Tafel slope analysis (predicted: 97.6 mV dec^{-1} for CAT_06928) quantifies reaction kinetics and rate-determining step confirmation.

Phase 3 - Mechanistic confirmation: Operando Raman and synchrotron X-ray absorption spectroscopy validate predicted *COCO intermediate binding energies ($\Delta E_{ads} = -0.82$ eV) and C-C coupling pathway activation. Isotope labeling experiments using $^{13}CO_2$ and D_2O confirm reaction mechanisms and intermediate formation sequences. Comparative DFT calculations on experimentally synthesized catalysts using identical VASP parameters (PBE-GGA functional, 4 ×4 ×1 k-point mesh, 500 eV cutoff) enable direct computational-experimental benchmarking, quantifying DFT prediction accuracy and identifying systematic deviations requiring functional corrections.

Phase 4 - Scale-up performance assessment: Pilot-scale electrochemical reactors (1–10 L working volume) validate predicted performance retention at industrial-relevant scales. The computational framework predicts 82% Faradaic efficiency retention scaling from laboratory H-cells to 10 m^3 reactors. Experimental scale-up testing quantifies mass transport limitations, electrode geometry effects, electrolyte management requirements, and thermal control strategies not captured in idealized computational models. Integration with CO_2 capture systems validates end-to-end process viability and refines techno-economic projections with experimental cost data.

Adaptive implementation strategy: The computational framework provides 301 Pareto-optimal catalyst configurations enabling flexible experimental implementation. If synthesis constraints limit maximum heteroatom concentrations below 7.3 at%, alternative candidates such as CAT_02907 (2.04 at% doping) maintain predicted C_{2+} Faradaic efficiencies above 78% while simplifying synthesis protocols. Experimental performance data enable Bayesian machine learning model refinement, progressively improving prediction accuracy through iterative computational-experimental cycles. Significant deviations between predicted and measured performance (e.g., experimental FE = 70% vs. predicted 89.5%) inform DFT functional selection, solvation model improvements, and expanded training dataset requirements for subsequent screening campaigns.

This validation strategy establishes experimentally verified design principles for heteroatom-doped carbon electrocatalysts, bridging computational discovery with industrial CO_2 utilization technologies.

7. Conclusion

This investigation develops an integrated computational framework combining high-throughput density functional theory screening of 8000 catalyst configurations with ensemble machine learning (cross-validated R^2=0.8760 ± 0.0274) to identify promising defect-engineered heteroatom-doped carbon electrocatalyst candidates for selective CO_2 electroreduction to C_{2+} products. Computational analysis suggests that ternary N-S-P doping at 7.3 at% concentration combined with Stone-Wales defect density of 4.6% generates synergistic electronic modulation predicted to maintain near-thermoneutral binding energies across reaction intermediates while optimizing C-C coupling barriers within the thermodynamically favorable 0.5–0.75 eV window. The computationally highest-performing candidate (CAT_06928) is predicted to achieve 89.5 ± 1.7% C_{2+} Faradaic efficiency at 301 ± 9 mA cm^{-2} with projected operational costs below $0.50 per kg, representing a predicted improvement over current experimental benchmarks pending experimental validation.

The demonstrated integration of DFT thermodynamics, microkinetic modeling, and machine learning prediction establishes a systematic approach for accelerating catalyst discovery beyond trial-and-error empiricism. Feature importance analysis revealing *COCO intermediate adsorption energy as the dominant descriptor (importance = 0.1471) and Pareto optimization identifying 301 configurations balancing activity-selectivity-stability trade-offs provide quantitative design principles for experimental catalyst development. However, these computational predictions require rigorous experimental validation through synthesis, electrochemical characterization, and operando spectroscopy before definitive performance claims can be established.

By providing computationally optimized catalyst candidates with predicted pilot-scale performance retention and economic competitiveness, this investigation contributes a data-driven roadmap toward bridging the technology translation gap limiting electrochemical CO_2 utilization deployment. The framework's generalizability extends to other multielectron electrocatalytic transformations including nitrogen fixation and oxygen reduction, positioning artificial intelligence-accelerated computational materials discovery as a promising strategy for sustainable chemical manufacturing technologies.

Author contributions

M.F.R. conceived the study, designed the methodology, conducted data collection and analysis, developed the computational framework, performed model validation, interpreted results, and wrote the manuscript.

CRediT authorship contribution statement

Mohammad Fazle Rabbi: Writing – review & editing, Writing – original draft, Visualization, Validation, Supervision, Software, Resources, Project administration, Methodology, Investigation, Funding acquisition, Formal analysis, Data curation, Conceptualization.

Informed consent statement

Not applicable.

Declaration of Generative AI and AI-assisted technologies in the writing process

During preparation of this manuscript, DeepL Write and ScienceDirect AI were utilized exclusively for language refinement, grammar correction, academic tone enhancement, and manuscript formatting. DeepL Write provided sentence-level writing improvements and clarity enhancements. ScienceDirect AI assisted with literature search refinement and related terminology accuracy. All research design, methodology, data analysis, result interpretation, and scientific conclusions were entirely conceived, executed, and verified by the author. Following application of these tools, the manuscript was thoroughly reviewed and edited to ensure all content reflects the author's original work and

scientific intent. The author assumes full responsibility for the accuracy, integrity, and scientific validity of this publication.

Funding

This research received no external funding.

Institutional Review Board Statement

Not applicable.

Declaration of Competing Interest

The authors declare the following financial interests/personal relationships which may be considered as potential competing interests: Mohammad Fazle Rabbi reports administrative support and article publishing charges were provided by University of Debrecen. If there are other authors, they declare that they have no known competing financial interests or personal relationships that could have appeared to influence the work reported in this paper.

Acknowledgments

This research was supported by the “University of Debrecen Program for Scientific Publication”.

Appendix A. Supporting information

Supplementary data associated with this article can be found in the online version at doi:10.1016/j.jcou.2026.103432.

Data availability

All computational datasets generated during this study (27 CSV files) are provided as Supplementary Data Files submitted with this manuscript. Complete nomenclature and abbreviations are provided in Appendix A.

References

[1] P. Friedlingstein, M. O'Sullivan, M.W. Jones, R.M. Andrew, D.C.E. Bakker, J. Hauck, P. Landschützer, C. Le Quéré, I.T. Luijkx, G.P. Peters, W. Peters, J. Pongratz, C. Schwingshackl, S. Sitch, J.G. Canadell, P. Ciais, R.B. Jackson, S. R. Alin, P. Anthoni, L. Barbero, N.R. Bates, M. Becker, N. Bellouin, B. Decharme, L. Bopp, I.B.M. Brasika, P. Cadule, M.A. Chamberlain, N. Chandra, T.-T.-T. Chau, F. Chevallier, L.P. Chini, M. Cronin, X. Dou, K. Enyo, W. Evans, S. Falk, R.A. Feely, L. Feng, D.J. Ford, T. Gasser, J. Ghattas, T. Gkritzalis, G. Grassi, L. Gregor, N. Gruber, Ö. Gürses, I. Harris, M. Hefner, J. Heinke, R.A. Houghton, G.C. Hurtt, Y. Iida, T. Ilyina, A.R. Jacobson, A. Jain, T. Jarníková, A. Jersild, F. Jiang, Z. Jin, F. Joos, E. Kato, R.F. Keeling, D. Kennedy, K. Klein Goldewijk, J. Knauer, J. I. Korsbakken, A. Körtzinger, X. Lan, N. Lefèvre, H. Li, J. Liu, Z. Liu, L. Ma, G. Marland, N. Mayot, P.C. McGuire, G.A. McKinley, G. Meyer, E.J. Morgan, D. R. Munro, S.-I. Nakaoka, Y. Niwa, K.M. O'Brien, A. Olsen, A.M. Omar, T. Ono, M. Paulsen, D. Pierrot, K. Pocock, B. Poulter, C.M. Powis, G. Rehder, L. Resplandy, E. Robertson, C. Rödenbeck, T.M. Rosan, J. Schwinger, R. Séférian, T.L. Smallman, S.M. Smith, R. Sospedra-Alfonso, Q. Sun, A.J. Sutton, C. Sweeney, S. Takao, P. P. Tans, H. Tian, B. Tilbrook, H. Tsujino, F. Tubiello, G.R. van der Werf, E. van Ooijen, R. Wanninkhof, M. Watanabe, C. Wimart-Rousseau, D. Yang, X. Yang, W. Yuan, X. Yue, S. Zaehle, J. Zeng, B. Zheng, Global Carbon Budget 2023, Earth Syst. Sci. Data 15 (2023) 5301–5369, https://doi.org/10.5194/essd-15-5301-2023.

[2] M.F. Rabbi, Optimizing carbon emissions and SDG-12 performance in the EU food system, Carbon Res. 4 (2025), https://doi.org/10.1007/s44246-025-00220-w.

[3] Z. Liu, Z. Deng, S.J. Davis, P. Ciais, Global carbon emissions in 2023, Nat. Rev. Earth Environ. 5 (2024) 253–254, https://doi.org/10.1038/s43017-024-00532-2.

[4] M.F. Rabbi, S. Kovács, Quantifying global warming potential variations from greenhouse gas emission sources in forest ecosystems, Carbon Res. 3 (2024) 70, https://doi.org/10.1007/s44246-024-00156-7.

[5] R. Bai, W. Wang, W. Gao, M. Yang, X. Zhang, C. Wang, Z. Fan, L. Yang, Z. Zhang, X. Yan, Dynamically cross-linked oligo[2]rotaxane networks mediated by metal-coordination, Angew. Chem. Int. Ed. 63 (2024) e202410127, https://doi.org/10.1002/anie.202410127.

[6] M.F. Rabbi, Cross-framework hybrid artificial intelligence for high-penetration renewable energy integration: Multi-regional forecasting and adaptive control, Appl. Energy 401 (2025) 126834, https://doi.org/10.1016/j.apenergy.2025.126834.

[7] Y.Y. Birdja, E. Pérez-Gallent, M.C. Figueiredo, A.J. Göttle, F. Calle-Vallejo, M.T. M. Koper, Advances and challenges in understanding the electrocatalytic conversion of carbon dioxide to fuels, Nat. Energy 4 (2019) 732–745, https://doi.org/10.1038/s41560-019-0450-y.

[8] P. De Luna, C. Hahn, D. Higgins, S.A. Jaffer, T.F. Jaramillo, E.H. Sargent, What would it take for renewably powered electrosynthesis to displace petrochemical processes? Science 364 (1979) (2019) eaav3506 https://doi.org/10.1126/science.aav3506.

[9] Z.W. Seh, J. Kibsgaard, C.F. Dickens, I. Chorkendorff, J.K. Nørskov, T.F. Jaramillo, Combining theory and experiment in electrocatalysis: Insights into materials design, Science 355 (1979) (2017) eaad4998, https://doi.org/10.1126/science.aad4998.

[10] M. Liu, Q. Wang, T. Luo, M. Herran, X. Cao, W. Liao, L. Zhu, H. Li, A. Stefancu, Y.-R. Lu, T.-S. Chan, E. Pensa, C. Ma, S. Zhang, R. Xiao, E. Cortés, Potential alignment in tandem catalysts enhances CO2-to-C2 H4 Conversion Efficiencies, J. Am. Chem. Soc. 146 (2024) 468–475, https://doi.org/10.1021/jacs.3c09632.

[11] J.H. Thierer, O. Foresti, P.K. Yadav, M.H. Wilson, T.O.C. Moll, M.-C. Shen, E. M. Busch-Nentwich, M. Morash, K.L. Mohlke, J.F. Rawls, V. Malhotra, M. M. Hussain, S.A. Farber, Pla2g12b drives expansion of triglyceride-rich lipoproteins, Nat. Commun. 15 (2024) 2095, https://doi.org/10.1038/s41467-024-46102-4.

[12] S. Nitopi, E. Bertheussen, S.B. Scott, X. Liu, A.K. Engstfeld, S. Horch, B. Seger, I.E. L. Stephens, K. Chan, C. Hahn, J.K. Nørskov, T.F. Jaramillo, I. Chorkendorff, Progress and Perspectives of Electrochemical CO2 Reduction on Copper in Aqueous Electrolyte, Chem. Rev. 119 (2019) 7610–7672, https://doi.org/10.1021/acs.chemrev.8b00705.

[13] S. Fu, M. Li, W. de Jong, R. Kortlever, Tuning the Properties of N-Doped Biochar for Selective CO2 Electroreduction to CO, ACS Catal. 13 (2023) 10309–10323, https://doi.org/10.1021/acscatal.3c01773.

[14] X. Chen, L. Liu, P.Y. Yu, S.S. Mao, Increasing solar absorption for photocatalysis with black hydrogenated titanium dioxide nanocrystals, Science 331 (1979) (2011) 746–750, https://doi.org/10.1126/science.1200448.

[15] M.F. Rabbi, Optimizing Carbon capture efficiency: knowledge extraction from process simulations of post-combustion amine scrubbing, Mach. Learn. Knowl. Extr. 8 (2026) 87, https://doi.org/10.3390/make8040087.

[16] J. Wu, S. Ma, J. Sun, J.I. Gold, C. Tiwary, B. Kim, L. Zhu, N. Chopra, I.N. Odeh, R. Vajtai, A.Z. Yu, R. Luo, J. Lou, G. Ding, P.J.A. Kenis, P.M. Ajayan, A metal-free electrocatalyst for carbon dioxide reduction to multi-carbon hydrocarbons and oxygenates, Nat. Commun. 7 (2016) 13869, https://doi.org/10.1038/ncomms13869.

[17] B. Pan, X. Zhu, Y. Wu, T. Liu, X. Bi, K. Feng, N. Han, J. Zhong, J. Lu, Y. Li, Y. Li, Toward Highly Selective Electrochemical CO2 Reduction using Metal-Free Heteroatom-Doped Carbon, Adv. Sci. 7 (2020) 2001002, https://doi.org/10.1002/advs.202001002.

[18] S. Back, J. Yoon, N. Tian, W. Zhong, K. Tran, Z.W. Ulissi, Convolutional Neural Network of Atomic Surface Structures To Predict Binding Energies for High-Throughput Screening of Catalysts, J. Phys. Chem. Lett. 10 (2019) 4401–4408, https://doi.org/10.1021/acs.jpclett.9b01428.

[19] X. Ma, Z. Li, L.E.K. Achenie, H. Xin, Machine-Learning-Augmented Chemisorption Model for CO2 Electroreduction Catalyst Screening, J. Phys. Chem. Lett. 6 (2015) 3528–3533, https://doi.org/10.1021/acs.jpclett.5b01660.

[20] X. Liu, J. Xiao, H. Peng, X. Hong, K. Chan, J.K. Nørskov, Understanding trends in electrochemical carbon dioxide reduction rates, Nat. Commun. 8 (2017) 15438, https://doi.org/10.1038/ncomms15438.

[21] S. Grimme, S. Ehrlich, L. Goerigk, Effect of the damping function in dispersion corrected density functional theory, J. Comput. Chem. 32 (2011) 1456–1465, https://doi.org/10.1002/jcc.21759.

[22] D.H. Mok, H. Li, G. Zhang, C. Lee, K. Jiang, S. Back, Data-driven discovery of electrocatalysts for CO2 reduction using active motifs-based machine learning, Nat. Commun. 14 (2023) 7303, https://doi.org/10.1038/s41467-023-43118-0.

[23] Z. Gariepy, G. Chen, A. Xu, Z. Lu, Z.W. Chen, C.V. Singh, Machine learning assisted binary alloy catalyst design for the electroreduction of CO2 to C2 products, Energy Adv. 2 (2023) 410–419, https://doi.org/10.1039/D2YA00316C.

[24] R. Ma, K. Wang, C. Li, C. Wang, A. Habibi-Yangjeh, G. Shan, N-doped graphene for electrocatalytic O2 and CO2 reduction, Nanoscale Adv. 4 (2022) 4197–4209, https://doi.org/10.1039/D2NA00348A.

[25] J. Li, X. Lu, Y. Chen, Y. Zhong, J. Yao, J. Wang, X. Wang, Machine learning-guided high-throughput screening of dual-atom catalysts for electrochemical C-C coupling, Chem. Eng. Sci. 320 (2026) 122415, https://doi.org/10.1016/j.ces.2025.122415.

[26] F. Pan, B. Li, W. Deng, Z. Du, Y. Gang, G. Wang, Y. Li, Promoting electrocatalytic CO2 reduction on nitrogen-doped carbon with sulfur addition, Appl. Catal. B 252 (2019) 240–249, https://doi.org/10.1016/j.apcatb.2019.04.025.

[27] A. Cho, B.J. Park, J.W. Han, Computational screening of single-metal-atom embedded graphene-based electrocatalysts stabilized by heteroatoms, Front. Chem. 10 (2022), https://doi.org/10.3389/fchem.2022.873609.

[28] H. Cabrera-Tinoco, L. Borja-Castro, R. Valencia-Bedregal, A. Perez-Carreño, A. Lalupu-García, I. Veliz-Quiñones, A.G. Bustamante Dominguez, C.H.W. Barnes, L. De Los Santos Valladares, Pyridinic-N coordination effect on the adsorption and activation of CO2 by single vacancy iron-doped graphene, Langmuir 40 (2024) 6703–6717, https://doi.org/10.1021/acs.langmuir.3c03327.

[29] K. Khan, X. Yan, Q. Yu, S.-H. Bae, J.J. White, J. Liu, T. Liu, C. Sun, J. Kim, H.-M. Cheng, Y. Wang, B. Liu, K. Amine, X. Pan, Z. Luo, Stone-Wales defect-rich carbon-supported dual-metal single atom sites for Zn-air batteries, Nano Energy 90 (2021) 106488, https://doi.org/10.1016/j.nanoen.2021.106488.

[30] A. Liu, Y. Yang, D. Kong, X. Ren, M. Gao, X. Liang, Q. Yang, J. Zhang, L. Gao, T. Ma, DFT study of the defective carbon materials with vacancy and heteroatom as catalyst for NRR, Appl. Surf. Sci. 536 (2021) 147851, https://doi.org/10.1016/j.apsusc.2020.147851.

[31] O. Leenaerts, B. Partoens, F.M. Peeters, Adsorption of H2 O, N H3, CO, N O2, and NO on graphene: A first-principles study, Phys. Rev. B 77 (2008) 125416, https://doi.org/10.1103/PhysRevB.77.125416.

[32] D. Yuan, Y. Zhang, W. Ho, R. Wu, Effects of van der Waals Dispersion Interactions in Density Functional Studies of Adsorption, Catalysis, and Tribology on Metals, J. Phys. Chem. C. 124 (2020) 16926–16942, https://doi.org/10.1021/acs.jpcc.0c02293.

[33] J.K. Nørskov, J. Rossmeisl, A. Logadottir, L. Lindqvist, J.R. Kitchin, T. Bligaard, H. Jónsson, Origin of the Overpotential for Oxygen Reduction at a Fuel-Cell Cathode, J. Phys. Chem. B 108 (2004) 17886–17892, https://doi.org/10.1021/jp047349j.

[34] L. Breiman, Random Forests, Mach. Learn 45 (2001) 5–32, https://doi.org/10.1023/A:1010933404324.

[35] J.H. Friedman, Greedy function approximation: a gradient boosting machine, Ann. Stat. 29 (2001) 1189–1232, https://doi.org/10.1214/aos/1013203451.

[36] T. Chen, C. Guestrin, XGBoost. Proceedings of the 22nd ACM SIGKDD International Conference on Knowledge Discovery and Data Mining, ACM, New York, NY, USA, 2016, pp. 785–794, https://doi.org/10.1145/2939672.2939785.

[37] D.P. Kingma, J. Ba, Adam: A Method for Stochastic Optimization, (2017). ⟨http://arxiv.org/abs/1412.6980⟩.

[38] T. Akiba, S. Sano, T. Yanase, T. Ohta, M. Koyama, Optuna. Proceedings of the 25th ACM SIGKDD International Conference on Knowledge Discovery & Data Mining, ACM, New York, NY, USA, 2019, pp. 2623–2631, https://doi.org/10.1145/3292500.3330701.

[39] G. Zhang, Z.-J. Zhao, D. Cheng, H. Li, J. Yu, Q. Wang, H. Gao, J. Guo, H. Wang, G. A. Ozin, T. Wang, J. Gong, Efficient CO2 electroreduction on facet-selective copper films with high conversion rate, Nat. Commun. 12 (2021) 5745, https://doi.org/10.1038/s41467-021-26053-w.

[40] S. Liang, J. Xiao, T. Zhang, Y. Zheng, Q. Wang, B. Liu, Sulfur Changes the Electrochemical CO2 Reduction Pathway over Cu Electrocatalysts, Angew. Chem. Int. Ed. 62 (2023) e202310740, https://doi.org/10.1002/anie.202310740.

[41] J. Mitra, S. Jain, A. Sharma, B. Basu, Patterned growth and differentiation of neural cells on polymer derived carbon substrates with micro/nano structures in vitro, Carbon N. Y 65 (2013) 140–155, https://doi.org/10.1016/j.carbon.2013.08.008.

[42] G. Hasegawa, T. Deguchi, K. Kanamori, Y. Kobayashi, H. Kageyama, T. Abe, K. Nakanishi, High-level doping of nitrogen, phosphorus, and sulfur into activated carbon monoliths and their electrochemical capacitances, Chem. Mater. 27 (2015) 4703–4712, https://doi.org/10.1021/acs.chemmater.5b01349.

[43] B. Efron, R.J. Tibshirani, An Introduction to the Bootstrap, Chapman and Hall/CRC, 1994, https://doi.org/10.1201/9780429246593.

[44] S. Osella, W.A. Goddard III, CO2 reduction to methane and ethylene on a single-atom catalyst: a grand canonical quantum mechanics study, J. Am. Chem. Soc. 145 (2023) 21319–21329, https://doi.org/10.1021/jacs.3c05650.

[45] J.G. Kirkwood, Statistical mechanics of fluid mixtures, J. Chem. Phys. 3 (1935) 300–313, https://doi.org/10.1063/1.1749657.

[46] M. Bonomi, D. Branduardi, G. Bussi, C. Camilloni, D. Provasi, P. Raiteri, D. Donadio, F. Marinelli, F. Pietrucci, R.A. Broglia, M. Parrinello, PLUMED: A portable plugin for free-energy calculations with molecular dynamics, Comput. Phys. Commun. 180 (2009) 1961–1972, https://doi.org/10.1016/j.cpc.2009.05.011.

[47] H. Zhong, H. Yao, J. Duo, G. Yao, F. Jin, Pd/C-catalyzed reduction of NaHCO 3 into CH 3 COOH with water as a hydrogen source, Catal. Today 274 (2016) 28–34, https://doi.org/10.1016/j.cattod.2016.05.010.

[48] D.N. LeBard, D.V. Matyushov, Redox entropy of plastocyanin: Developing a microscopic view of mesoscopic polar solvation, J. Chem. Phys. 128 (2008) 155106, https://doi.org/10.1063/1.2904879.

[49] K. Mathew, R. Sundararaman, K. Letchworth-Weaver, T.A. Arias, R.G. Hennig, Implicit solvation model for density-functional study of nanocrystal surfaces and reaction pathways, J. Chem. Phys. 140 (2014), https://doi.org/10.1063/1.4865107.

[50] F. Abild-Pedersen, J. Greeley, F. Studt, J. Rossmeisl, T.R. Munter, P.G. Moses, E. Skúlason, T. Bligaard, J.K. Nørskov, Scaling properties of adsorption energies for hydrogen-containing molecules on transition-metal surfaces, Phys. Rev. Lett. 99 (2007) 016105, https://doi.org/10.1103/PhysRevLett.99.016105.

[51] X. Gonze, C. Lee, Dynamical matrices, Born effective charges, dielectric permittivity tensors, and interatomic force constants from density-functional perturbation theory, Phys. Rev. B 55 (1997) 10355–10368, https://doi.org/10.1103/PhysRevB.55.10355.

[52] K. Tong, F. You, G. Rong, Robust design and operations of hydrocarbon biofuel supply chain integrating with existing petroleum refineries considering unit cost objective, Comput. Chem. Eng. 68 (2014) 128–139, https://doi.org/10.1016/j.compchemeng.2014.05.003.

[53] W.A. Smith, T. Burdyny, D.A. Vermaas, H. Geerlings, Pathways to Industrial-Scale Fuel Out of Thin Air from CO2 Electrolysis, Joule 3 (2019) 1822–1834, https://doi.org/10.1016/j.joule.2019.07.009.

[54] G. Wernet, C. Bauer, B. Steubing, J. Reinhard, E. Moreno-Ruiz, B. Weidema, The ecoinvent database version 3 (part I): overview and methodology, Int. J. Life Cycle Assess. 21 (2016) 1218–1230, https://doi.org/10.1007/s11367-016-1087-8.

[55] Argonne National Laboratory, Argonne GREET R&D Model, (2025). ⟨https://greet.anl.gov/⟩ (accessed January 19, 2026).

[56] J.W. Tukey, Comparing individual means in the analysis of variance, Biometrics 5 (1949) 99, https://doi.org/10.2307/3001913.

[57] T. Developers, TensorFlow (2025), https://doi.org/10.5281/ZENODO.16852354.

[58] G. Kresse, J. Hafner, Ab initio molecular dynamics for liquid metals, Phys. Rev. B 47 (1993) 558–561, https://doi.org/10.1103/PhysRevB.47.558.

[59] J.P. Perdew, K. Burke, M. Ernzerhof, Generalized gradient approximation made simple, Phys. Rev. Lett. 77 (1996) 3865–3868, https://doi.org/10.1103/PhysRevLett.77.3865.

[60] P.E. Blöchl, Projector augmented-wave method, Phys. Rev. B 50 (1994) 17953–17979, https://doi.org/10.1103/PhysRevB.50.17953.

[61] M. Matsumoto, T. Nishimura, Mersenne twister, ACM Trans. Model. Comput. Simul. 8 (1998) 3–30, https://doi.org/10.1145/272991.272995.

[62] R. Amirbeigiarab, J. Tian, A. Herzog, C. Qiu, A. Bergmann, B. Roldan Cuenya, O. M. Magnussen, Atomic-scale surface restructuring of copper electrodes under CO2 electroreduction conditions, Nat. Catal. 6 (2023) 837–846, https://doi.org/10.1038/s41929-023-01009-z.

[63] D. Nam, O. Shekhah, A. Ozden, C. McCallum, F. Li, X. Wang, Y. Lum, T. Lee, J. Li, J. Wicks, A. Johnston, D. Sinton, M. Eddaoudi, E.H. Sargent, High-Rate and Selective CO2 electrolysis to ethylene via metal–organic-framework-augmented CO2 Availability, Adv. Mater. 34 (2022), https://doi.org/10.1002/adma.202207088.

[64] Q. Fang, Y. Jia, X. Lang, G. Li, T. Zhao, D. Zhong, J. Li, Q. Zhao, Defect-Rich Porous Cu with Abundant Cu(100) for Acidic CO $_2$ Electroreduction in Membrane Electrode Assembly, Adv. Sci. 12 (2025), https://doi.org/10.1002/advs.202510161.

[65] M.F. Rabbi, Accelerating Green Innovation Dynamics: Cross-Scale Modelling of Technology Competition and Institutional Inertia, J. Open Innov. Technol. Mark. Complex. (2026) 100760, https://doi.org/10.1016/j.joitmc.2026.100760.

[66] L. Zhang, Y. Yang, L. Zhou, F. Zhao, H. Cheng, Reductive amination of 1,6-hexanediol with a modified Ru/Al2O3 catalyst, Appl. Catal. A Gen. 669 (2024) 119509, https://doi.org/10.1016/j.apcata.2023.119509.

[67] X. Cao, W. Luo, H. Liu, A prediction model for CO2 /CO adsorption performance on binary alloys based on machine learning, RSC Adv. 14 (2024) 12235–12246, https://doi.org/10.1039/D4RA00710G.

[68] S. Bhardwaj, S.J. Alli, N. Barman, R. Thapa, R.S. Dey, Ternary Heteroatom-doped carbon as a high-performance metal-free catalyst for electrochemical ammonia synthesis, ACS Appl. Mater. Interfaces 17 (2025) 26661–26670, https://doi.org/10.1021/acsami.5c02039.

[69] Y. Gao, Q. Wang, G. Ji, A. Li, J. Niu, Doping strategy, properties and application of heteroatom-doped ordered mesoporous carbon, RSC Adv. 11 (2021) 5361–5383, https://doi.org/10.1039/D0RA08993A.

[70] S.A. Chambers, Epitaxial growth and properties of thin film oxides, Surf. Sci. Rep. 39 (2000) 105–180, https://doi.org/10.1016/S0167-5729(00)00005-4.

[71] D. Wakerley, S. Lamaison, F. Ozanam, N. Menguy, D. Mercier, P. Marcus, M. Fontecave, V. Mougel, Bio-inspired hydrophobicity promotes CO2 reduction on a Cu surface, Nat. Mater. 18 (2019) 1222–1227, https://doi.org/10.1038/s41563-019-0445-x.

[72] Y. Bao, J. Ni, C. Qiu, A minimalist single-layer metasurface for arbitrary and full control of vector vortex beams, Adv. Mater. 32 (2020) 1905659, https://doi.org/10.1002/adma.201905659.

[73] W. Dai, S. Li, H. Jia, X. Zhao, C. Liu, C. Zhou, Y. Xiao, L. Guo, Y. Fan, X. Zhang, Indirect 3D printing CDHA scaffolds with hierarchical porous structure to promote osteoinductivity and bone regeneration, J. Mater. Sci. Technol. 207 (2025) 295–307, https://doi.org/10.1016/j.jmst.2024.04.032.

[74] Z. Wu, E. Zhu, Y. Xing, P. Huang, B. Li, L. Liu, Magnetic modulation to construct MXene/CNT@Fe3O4 electrodes with 3D conductive structures for ionic artificial muscles, Carbon N. Y 221 (2024) 118953, https://doi.org/10.1016/j.carbon.2024.118953.

[75] A. Rao, V. Gustin, J. Hightower, S. Gunduz, D. Basu, Y. Khalifa, A. Sohale, A.C. Co, A. Asthagiri, U.S. Ozkan, CO2 Poisoning of CNx Catalysts for the Oxygen Reduction Reaction, J. Phys. Chem. C. 129 (2025) 379–390, https://doi.org/10.1021/acs.jpcc.4c07363.

[76] J.-W. DuanMu, Z.-Z. Wu, F.-Y. Gao, P.-P. Yang, Z.-Z. Niu, Y.-C. Zhang, L.-P. Chi, M.-R. Gao, Investigation and mitigation of carbon deposition over copper catalyst during electrochemical CO2 Reduction, Precis. Chem. 2 (2024) 151–160, https://doi.org/10.1021/prechem.4c00002.

[77] T.N. Nguyen, Z. Chen, A.S. Zeraati, H.S. Shiran, S.Md Sadaf, M.G. Kibria, E. H. Sargent, C.-T. Dinh, Catalyst regeneration via chemical oxidation enables long-term electrochemical carbon dioxide reduction, J. Am. Chem. Soc. 144 (2022) 13254–13265, https://doi.org/10.1021/jacs.2c04081.

[78] Z.-X. Yuan, Y. Gao, S.-Q. Li, J. Xuan, X.-Y. Sheng, F. Zhang, Y. Zheng, P. Chen, A versatile catalyst in situ self-cleaning method for excellent cycling and operational stability in small-molecule electrooxidation, EScience 5 (2025) 100375, https://doi.org/10.1016/j.esci.2025.100375.